Response of Sandwich Structures to Blast Loads

Romesh C. Batra, Arka P. Chattopadhyay, and Priyal H. Shah

1 Introduction

An explosion in air or water instantaneously raises pressure in the medium adjacent to the blast that compresses the medium, results in a shock wave propagating in it, and applies an impulse load on a nearby structure. The resulting blast wave in air is called a blast wind [1]. An underwater explosion results in many subsequent phenomena that can cause catastrophic damage to a marine structure [2]. Early techniques of damaging a ship used underwater mines and torpedoes that exploded upon contacting the ship. However, by the end of the First World War, the effectiveness of a non-contact explosion in damaging a marine vessel was realized.

Rayleigh [3] studied cavitation in a gas bubble formed in an underwater explosion. Subsequently, Cole [4] characterized an underwater explosion and its interaction with marine structures. Taylor [5] studied the interaction of a blast wave from an underwater explosion with a wedge-type structure and a monolithic plate. Keil [2] discussed, in detail, the response of surface ships and submarines to underwater blasts that included the severity of damage to various components. Since then, experimental, analytical and computational research in underwater explosions has significantly advanced that has considered using composite laminates and sandwich structures to reduce the ship weight. Here, we first review some works on underwater explosion including gas bubble characteristics, shock wave propagation, cavitation phenomenon, and structural deformations, and then describe modeling and simulation of structural damage caused by shock loads.

R. C. Batra (✉) · A. P. Chattopadhyay · P. H. Shah
Department of Biomedical Engineering and Mechanics, M/C 0219, Virginia Polytechnic Institute and State University, Blacksburg, VA, USA
e-mail: rbatra@vt.edu

S. W. Lee (ed.), *Advances in Thick Section Composite and Sandwich Structures*,
https://doi.org/10.1007/978-3-030-31065-3_10

2 Loads Produced by Underwater Explosions

During the Second World War, the efficiency of a non-contact underwater explosion in disabling ships was realized thus triggering extensive research in this field.

2.1 Shock Wave

An underwater explosion results in a high-pressure superheated gas bubble centered at the explosion point. The bubble rapidly expands and creates a shock wave that initially travels at a speed much higher than the speed of sound, $c = 1.5$ km/s, in water. However, the shock wave speed rapidly drops to 1.5 km/s within a distance of 10 times the charge radius [2]. The shock wave propagates radially outwards and gets reflected from the sea free surface and the sea bottom. Rayleigh [3] characterized the velocity of bounding surfaces of an expanding bubble, the spherical cavity formed after an explosion, and the pressure in the bubble and on the surrounding fluid that was assumed to be incompressible. Deformations of the surrounding water are studied in [4] wherein it is stipulated that the exponential decay in time of the pressure, P, in the shock wave is given by

$$P = P_0 e^{-t/\theta}, \tag{1a}$$

$$P_0 = K_1 \left(\frac{W^{1/3}}{R_h} \right)^{A_1}, \tag{1b}$$

$$\theta = K_2 \left(W^{1/3} \right) \left(\frac{W^{1/3}}{R_h} \right)^{A_2} \tag{1c}$$

Here P_0 is the peak pressure at the explosion point, θ the decay constant, W the mass of the charge in kg, R_h the distance in meters of the point of interest (stand-off distance) from the explosion center, and K_1, K_2, A_1 and A_2 are constants. Values of these constants determined by Cole [4] from the test data for four explosives are listed in Table 1. Using these values, the pressure histories of the shock wave at R_h= 50 m are exhibited in Fig. 1. We note that for R_h< (10 times the charge radius) Eq. (1) considerably under-predicts P [6]. When the shock wave passes a fixed

Table 1 Values of constants in Eqs. (1b, 1c) for four explosives [4]

Explosive type	TNT	HBX – 1	PETN	Nuclear
K_1	52.12	53.31	56.21	1.06×10^4
K_2	1.18	1.144	1.194	1.13
A_1	0.0895	0.092	0.084	3.627
A_2	-0.185	-0.247	-0.257	-0.22

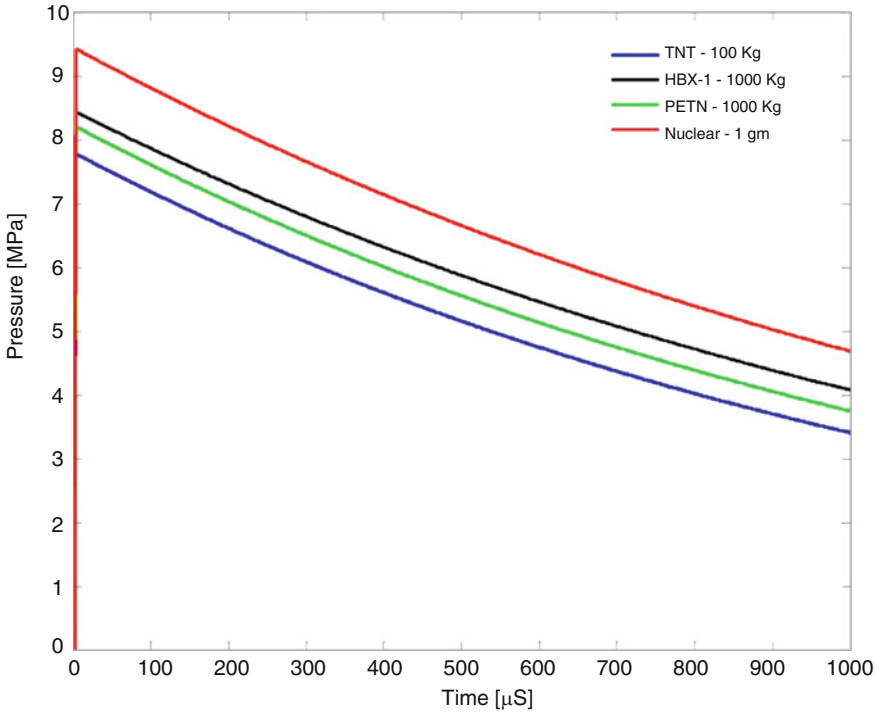

Fig. 1 For four explosives, time histories of the shock wave pressure at a stand-off distance of 50 m from the blast site

location in the liquid, particles there start flowing in the shock wave propagation direction at velocity *u(t)* given by

$$P(t) = \rho c u(t) \tag{2}$$

where ρ is the mass density of water. Keil [2] has suggested that due to the shock wave being spherical, Eq. (2) should be modified to

$$u(t) = \frac{P(t)}{\rho c} + \frac{1}{\rho R_h} \int_0^t P(t) dt \tag{3}$$

In Eq. (3), the first and the second terms, respectively, correspond to a planar and a spherical flow. In close proximity of the explosion, the second term significantly affects the particle velocity.

The total energy, because of the pressure and the particles velocity, associated with the shock wave is given by [4]

$$E_{sh} = \frac{1}{\rho c}\int_0^{\infty} P^2(t)dt, \tag{4a}$$

$$E_{sh} = \frac{1}{\rho c} P_0^2 \theta \tag{4b}$$

where we have substituted for $P(t)$ from Eq. (1).

Besides the pressure and the energy of a shock wave, its capacity to induce damage is measured by the total impulse of the wave. The impulse of a shock wave acting on a unit area at a point until time t can be expressed as

$$I = \int_0^t P(t)dt = P_0\theta \tag{5}$$

where we have used Eq. (1).

2.2 The Gas Bubble

After emission of the initial high pressure from the gas bubble in the form of a shock wave, the pressure in the gas remains higher than the surrounding hydrostatic pressure. Thus the bubble expands. However, due to inertia effects, the expansion does not stop at the equilibrium pressure and the bubble keeps expanding until the hydrostatic pressure exceeds the pressure of the gas in the bubble [7]. This contracts the bubble until its radius becomes the minimum. The bubble continues to oscillate around the equilibrium radius for many cycles; e.g., see Fig. 2. When the bubble reaches the minimum radius, a pressure pulse in the form of an aftershock, with the peak pressure of about 10–15% of the primary shock wave, is released.

$$R_{\max} = 3.3\left(\frac{W}{Z}\right)^{1/3}, \tag{6a}$$

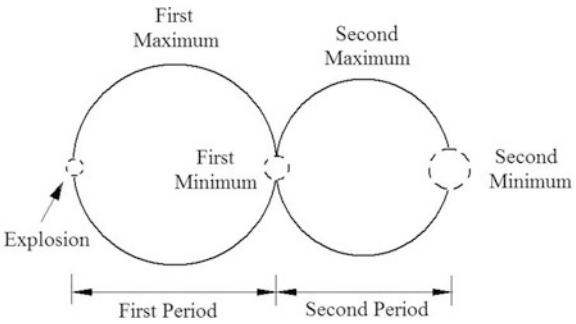

Fig. 2 Pulsation of gas bubble in an underwater explosion [4]

$$T = 2.08 \frac{W^{1/3}}{Z^{5/6}} \tag{6b}$$

In Eq. (6), $Z = D + 10$ is the total static pressure head at the explosion site, and D the depth of the explosion site in meters. Due to buoyancy force, the gas bubble migrates upwards towards the free surface. The migration rate reaches the maximum when the bubble radius reaches the minimum. For a TNT explosion, Reid [7] postulated the empirical expression (7), derived from test data, for the first migration, *mf*, from the explosion location to the place where the bubble radius reaches the first minimum.

$$mf = \frac{12.2}{Z} W^{1/3} \tag{7}$$

The migration distance from the first minimum to the second minimum is usually one-half of the distance calculated from Eq. (7). The bubble migration can cause extensive damage to ships in the migration path. The characteristic features of a gas bubble are summarized in Fig. 3.

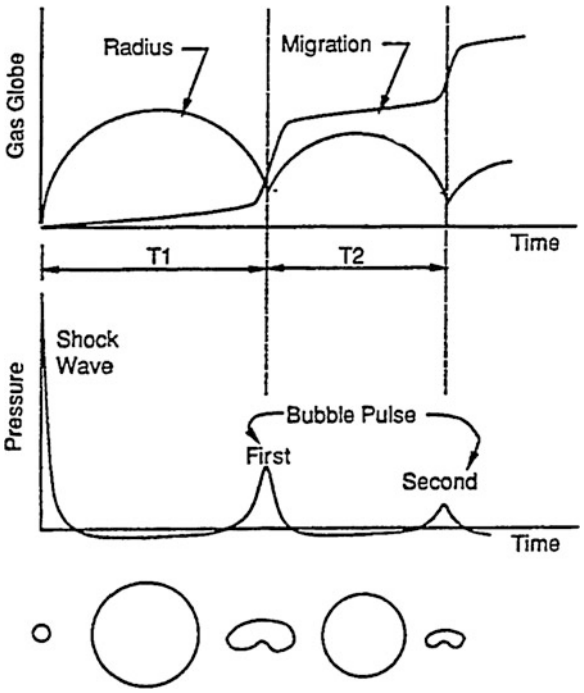

Fig. 3 Characteristics of a gas bubble at different times [4]

2.3 *Reflection of the Shock Wave from the Sea Surface and the Sea Bed*

The reflection of a shock wave from the sea surface and the sea bed is schematically represented in Fig. 4. The wave reflected from the sea surface (bed) is tensile (compressive). When the wave reflected from the sea bed (surface) interacts with the primary shock wave, it adds (subtracts) to the pressure of the primary wave. When the pressure temporarily becomes zero, the phenomenon is called surface cut-off. Keil's [2] empirical relation between the surface cut-off time, t_{zero}, and the position of the point is given by Eq. (8).

$$t_{zero} = \frac{0.122Dd}{R_h}, ms \tag{8}$$

In Eq. (8), d is the depth of the point, R_h the horizontal stand-off distance of the point from the blast location with d and R_h measured in meters.

When an explosion occurs at the sea bottom, the bubble develops as a hemisphere [4], and migrates along with the regular pulsation phenomenon [9].

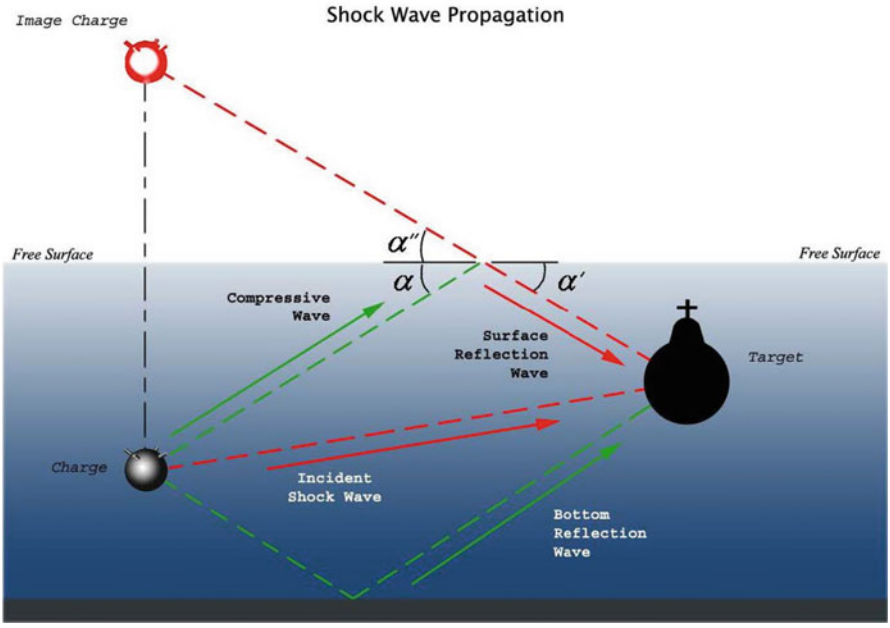

Fig. 4 Schematic representation of shock wave reflections [8]

2.4 Cavitation

Water cannot sustain tensile stresses. The bulk and the hull cavitation, respectively, ensue when stresses in a volume of water become tensile due to the interaction between the incident shock wave and that reflected from the sea surface or a structure. The bulk cavitation that is more likely to occur for an underwater explosion near the sea surface has been studied by Cole [4] and Snay [9]. Costanzo and Gordon [10] have calculated the extent and the duration of the cavitation process. The eventual closing of the cavitated region results in a water hammer and a pressure pulse called cavitation pulse [7]. The bulk cavitation occurring at the sea surface due to an underwater explosion is shown in Fig. 5.

A shock wave impinging upon a deformable ship hull accelerates the hull particles. When particles' velocities exceed the transient velocity of the adjacent volume of water, tensile tractions act on the water volume and ensue cavitation. This phenomenon is called hull cavitation, the maximum velocity of the hull is called the kick-off velocity [7], and has been studied by Cole [4] and Taylor [5].

Fig. 5 Bulk cavitation at the sea surface from an underwater explosion [4]

3 Response of Ships to an Underwater Explosion

Toward the end of the 2nd World War, it was realized that an underwater explosion can destroy ships. Keil [2] has discussed the response of ships based on experimental observations. Depending upon where an explosion occurs, they are classified as contact and non-contact type with the former (latter) having the explosion location adjacent (away) to either the ship hull or the ship bottom. In the former, either torpedoes or mines were used to tear open a 30–50 feet diameter hole on the ship exterior depending on the explosion type and size. The explosion also ruptures the ship bulkheads and the blast fragments heavily damage the machinery close to the explosion. Nurick and Martin [11, 12] have reviewed the literature on deformations of plates under loads typical of a contact explosion. Weirzbicki and Nurick [13] have experimentally and theoretically investigated deformations of plates under a localized impulsive loading. Assuming that the plate can be modeled as a membrane comprised of a perfectly plastic material and is deformed into a part of a sphere of radius ρ, we have [13]

$$(2\rho - \delta)\delta = R^2 \tag{9}$$

where δ is the maximum depth, and R the radius of the deformed plate along the undeformed surface; e.g., see Fig. 6. Cole [4] found R by equating the work, W, to the input energy, E_{in}, from the shock wave [14]. That is,

$$W = \sigma_y t_p \Delta A, \tag{10a}$$

$$R = \sqrt{\frac{2\eta E_{in}}{\pi t_p \sigma_y \varepsilon_f}}, \tag{10b}$$

$$E_{in} = W E_{TNT} E q_{TNT} J \tag{10c}$$

where η is the fraction of the E_{in} used to deform the plate, ($E_{def} = E_{in}\eta$), t_p the plate thickness, σ_y the yield stress of the plate material, ε_f the fracture strain, E_{TNT} the energy content of the TNT, E_{TNT} the TNT equivalent of the explosive used, and J the energy conversion factor. Rajendran and Lee [15] have reviewed contact explosion problems.

Figure 7 schematically shows characteristic dimensions associated with a non-contact underwater explosion for which the damage is mainly due to a shock

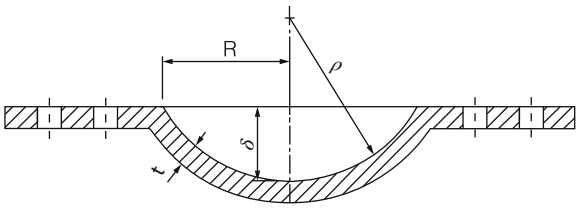

Fig. 6 Schematic representation of the deformation of a circular plate subjected to a contact explosion [14]

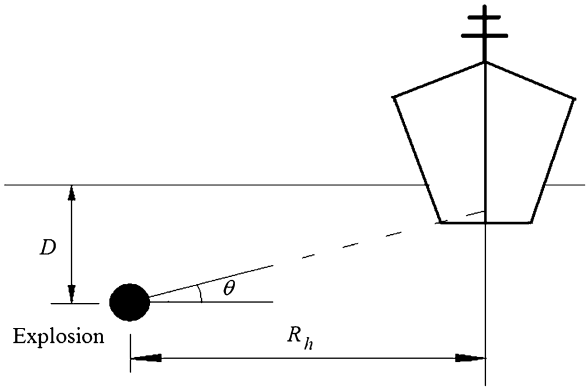

Fig. 7 Schematic representation of a non-contact underwater explosion

wave, bubble pulsation, bubble migration and cavitation. The impact of a shock wave on a ship hull requires analyzing fluid-structure interaction (FSI) between the water volume and the hull which can be simulated as an assembly of flat and curved plates.

One measure of the intensity of the shock wave at the hull is the Hull Shock Factor, HSF, [7], is given by

$$HSF = \frac{W_{eq}^{n}}{R_h} \tag{11}$$

where W_{eq} is the mass of the explosive used equivalent to the TNT and the parameter n, determined experimentally, depends on the explosive used and the explosion conditions. When the position of the explosion is measured with respect to the ship keel, the Keel Shock Factor, *KSF*, [7] for a shock wave making angle θ (see Fig. 7) with the horizontal line is defined as

$$KSF = HSF\left(\frac{1 + \sin\theta}{2}\right) \tag{12}$$

For explosions close to the ship hull, the damage is localized due to the spherical wave front that generally tears open a large hole similar to the damage caused by a contact explosion. For explosions at large stand-off distances, the incident shock wave is approximately planar, and deformations of different parts of the ship is generally dissimilar.

3.1 Fluid Structure Interaction of Monolithic Plates

Early works on studying the fluid-structure interaction (FSI) include those of Cole [4], Taylor [5] and Kennard [16]. When a traveling pressure pulse hits a ship hull, the

pulse is reflected back with some modifications caused due to the accelerating and deforming plate of the hull [6]. It is assumed that the plate is of infinite area based on the time scale of interaction of the pulse with the plate. For the incident pressure given by Eq. (1), the reflected wave pressure can be written as [4, 5]

$$P_r = P_0\varphi(t) \tag{13}$$

The total force acting on the plate is the sum of that due to the incident and the reflected pressure pulses. Assuming no separation between the water and the solid, at the water-plate interface the normal traction and the normal velocity must be continuous. However, the tangential velocity can be discontinuous for water modeled as inviscid. The plate deformations depend on support conditions at its rear surface and edges.

In the first approximation, the plate is modeled as a point, and its motion described by,

$$m\ddot{u} + c\dot{u} + ku = P_{net} \tag{14}$$

where m is the mass of the plate per unit area, a superimposed dot denotes the time derivative, c the damping coefficient, k the plate stiffness, P_{net} the net force per unit area, and u the plate displacement in the direction of the pressure pulse. The initial conditions are

$$u(0) = \dot{u}(0) = 0 \tag{15}$$

The solution of differential Eq. (14) provides the plate displacement and the velocity histories.

For an air backed plate (ABP), shown schematically in Fig. 8, the right face of the plate is subjected to air and does not resist motion. Using continuity conditions at the water-plate interface, the total pressure acting on the plate is found to be [4, 5]

$$P_{net}^{ABP} = 2P_0 e^{-t/\theta} - \rho c\dot{u} \tag{16}$$

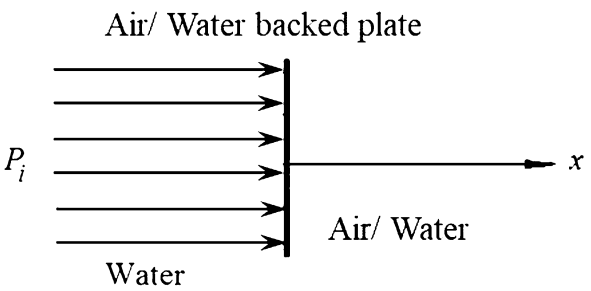

Fig. 8 Schematic representation of an air/water backed monolithic plate

where ρ is the mass density of water, and c is the sound speed in the plate. For the pressure pulse hitting a stationary rigid wall, $\dot{u}= 0$.

Substitution of the total pressure from Eq. (16) into Eq. (14) and using initial conditions described by Eq. (15) gives the following for the plate displacement and velocity [5, 17].

$$u_a = \frac{2P_0\theta}{m\psi(\psi-1)}\left[(\psi-1)+e^{-(\psi/\theta)t}-\psi e^{-t/\theta}\right], \tag{17a}$$

$$v_a = \dot{u}_a = \frac{2P_0\theta}{m(1-\psi)}\left(e^{-\psi t/\theta}-e^{-t/\theta}\right) \tag{17b}$$

The dimensionless quantity, $\psi = \rho c\theta/m$, is called the FSI parameter of an ABP. Substitution from Eq. (17) into Eq. (16) results in

$$P_{net}^{ABP} = 2P_0 e^{-t/\theta} - \frac{2P_0\psi}{(\psi-1)}(e^{-t/\theta}-e^{-\psi t/\theta}) \tag{18}$$

Recalling that the hull cavitation begins when the net pressure equals zero, the cavitation inception time, t_c^{ABP}, is [5, 17].

$$t_c^{ABP} = \theta\frac{\ln\psi}{\psi-1} \tag{19}$$

Another parameter of interest is the fraction of the maximum momentum transferred to the plate that occurs at the cavitation inception time when the plate has the maximum velocity. Thus, the plate maximum momentum, I_p, is given by

$$I_P = \zeta^{ABP} I_0, \zeta^{ABP} = \psi^{\psi/1-\psi} \tag{20}$$

where the free pulse momentum, I_0, is given by Eq. (5).

For a water backed plate (WBP), the water at the back of the plate exerts pressure on it and decreases the net force on the plate. The problem has been studied by Keil [2]. Proceeding in the same way as for the ABP, we get

$$u_w = \frac{2P_0\theta}{m\phi(\phi-1)}\left[(\phi-1)+e^{-(\phi/\theta t)}-\phi e^{-t/\theta}\right], \tag{21a}$$

$$v_w = \dot{u}_w = \frac{2P_0\theta}{m(1-\phi)}\left(e^{-\phi t/\theta}-e^{-t/\theta}\right) \tag{21b}$$

where $\phi = 2\psi = 2\rho c\theta/m$ is the FSI parameter for a WBP. Results for a WBP can be obtained from those for an ABP with ψ replaced by ϕ; e.g., see Liu and Young [18]. In Figs. 9 and 10, we have plotted time histories of the plate displacement, the plate velocity and the cavitation time for an ABP and a WBP. The characteristics of a WBP are important when designing liquid holding tanks close to a ship hull. When a

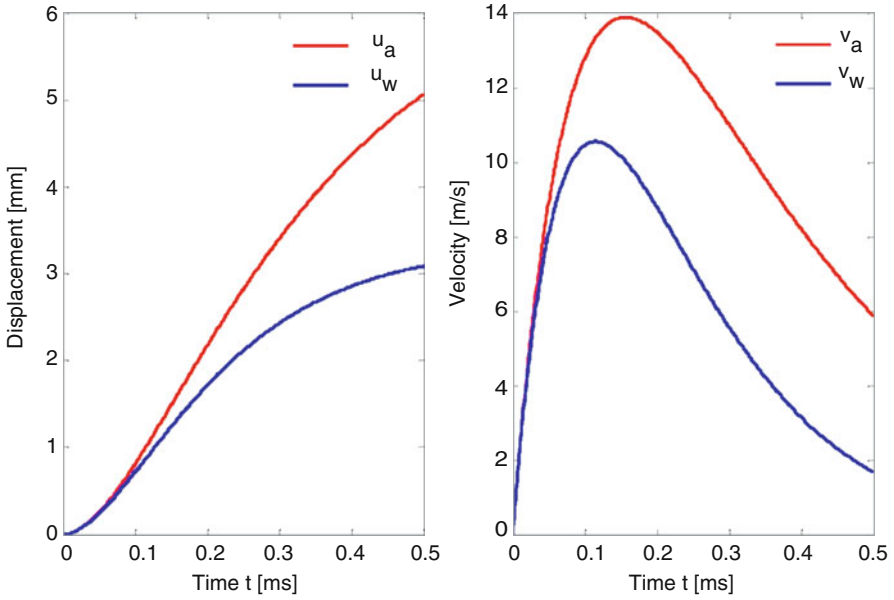

Fig. 9 The displacement and velocity histories of a plate with $\phi = 0.75$ and $\psi = 0.375$

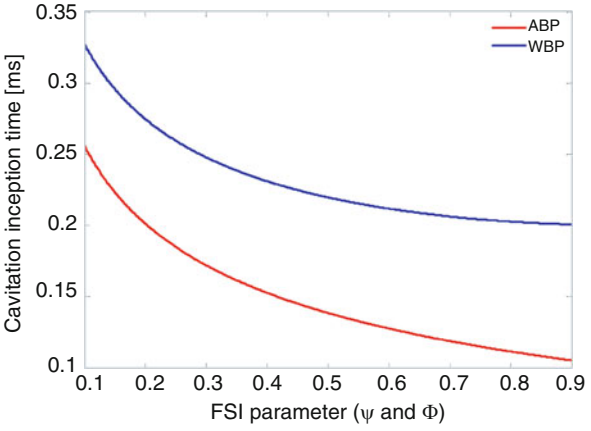

Fig. 10 Variation with the FSI parameter of the cavitation inception time for air- and water-backed plates

shock wave hits the outer wall of a tank, a part of the shock wave is transferred to the fluid inside the tank to generate another shock wave that can severely damage the internal wall. One way to avoid this is to not completely fill the tank that allows the shock wave energy to be converted to a free surface wave [7].

3.2 *Fluid Structure Interaction of Composite and Sandwich Plates*

Mouritz [19, 20] has experimentally studied the impact of glass fiber reinforced polymer (GRP) laminates including their fatigue behavior under increasing shock loads. The tests used large explosive charges at short stand-off distances for both ABP and WBP, and stitched and unstitched GRP laminates. He found that the damage caused to both stitched and unstitched laminates was similar. However, the damage and delamination in stitched laminates was less than that in unstitched specimens. At low (high) shock factors, the damage to Kevlar stitching threads was minimal (extensive).

Thick laminates respond differently to a shock wave than thin ones [21]. Morais et al. [22] experimentally studied the effect of the laminate thickness by dropping a weight on a clamped laminate. Gellert et al. [23] also experimentally studied the effect of the laminate thickness on its response to a shock wave. Several works [24–28] present experimental studies on the response of laminate plates to pressure pulses and delineate the effect on composites' deformations of fiber length, fiber/matrix interface and ply stacking sequence. Mouritz et al. [29] have reviewed composite structures used in ships and submarines.

Sandwich structures have a distinct advantage over monolithic plates in withstanding short time-duration shock wave pressure pulses [17, 30]. For the same areal density, a sandwich structure can sustain a more intense pressure pulse than a laminated plate. Fleck and Deshpande [17] used the relative time scales and the associated phenomena to divide the interaction of a metallic sandwich structure with a pressure pulse into three stages. In the first stage, the face plate hit by the shock wave is elastically compressed. In the second stage, the core is dynamically crushed and its initiation is marked by the cavitation inception time where the face plate achieves the maximum velocity which can be considered equivalent to the kick-off velocity of a monolithic plate. For an effective sandwich design, most of the incident energy is absorbed during core crushing [31]. The final stage involves global tearing and rupture of the face plate during which the remaining energy of the shock wave is absorbed. Figure 11 schematically shows phenomena occurring in the three stages [32].

Many researchers [16, 30–37] have analytically, numerically and experimentally studied deformations of a sandwich structure under a shock wave pressure pulse. In stage 1 of the interaction, the core stiffness resists motion of the face plate due to the impinging pressure pulse. For a core assumed to be rigid-perfectly plastic and having yield strength, σ_y, the motion of a unit area of the face plate is governed by [31]

$$m_f \ddot{u} = P(x,t) - \sigma_y \tag{22}$$

under null initial conditions (cf. Eq. (15)) and the resultant pressure $P(x, t)$ due to the incident and the reflected waves given by

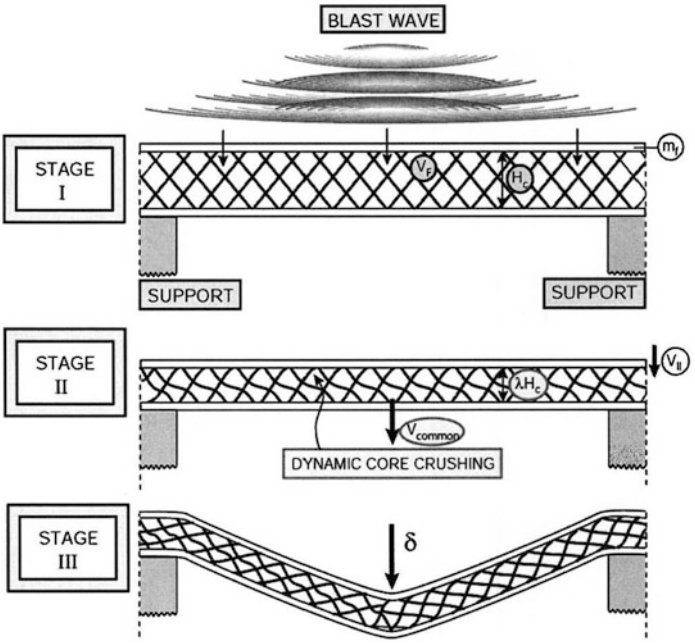

Fig. 11 Schematic representation of three stages of a blast wave-sandwich interaction [32]

$$P(x,t) = P_0\left(e^{\zeta} + e^{\xi}\right) - \rho c\dot{u}, \zeta = -t/\theta - x/c\theta, \xi = -t/\theta + x/c\theta \tag{23}$$

Fleck and Deshpande [17] have discussed the core yield strength as a function of the yield strength of the core material and the relative mass density of the core.

The solution of Eq. (22) under null initial conditions gives the following for the face plate displacement and velocity [35].

$$u = \frac{2P_0\theta}{m\psi(1-\psi)}\left[(1-\psi) - e^{-\psi t/\theta} + \psi e^{-t/\theta}\right] + \frac{\sigma_y\theta^2}{m\psi^2}\left(1 - e^{-\psi t/\theta} - \frac{\psi t}{\theta}\right) \tag{24}$$

$$\dot{u} = \frac{2P_0}{m(1-\psi)}\left(e^{-\psi t/\theta} - e^{-t/\theta}\right) + \frac{\sigma_y\theta}{m\psi}\left(e^{-\psi t/\theta} - 1\right) \tag{25}$$

For a monolithic (sandwich) plate, the spatial dependence of the pressure is ignored (considered) because the cavitation inception plane contacts (is away from) the plate surface.

The cavitation occurs when the face plate velocity is the maximum and the pressure in the fluid equals zero. By substituting from Eq. (25) into Eq. (23), we obtain the following expression for the fluid pressure as a function of space and time [35].

$$\frac{P}{P_0} = \frac{2}{1-\psi}\left(\cosh\widetilde{x} - \psi\sinh\widetilde{x}\right)e^{-\widetilde{t}} + \left(\frac{2\psi}{\psi-1}\right)e^{-\psi\widetilde{t}-\psi\widetilde{x}} - \widetilde{\sigma} \tag{26}$$

Here $\widetilde{x} = x/c\theta, \widetilde{t} = t/\theta$ and $\widetilde{\sigma} = \sigma_y/P_0$. The cavitation inception occurs when $P = 0$ and $\partial P/\partial\widetilde{x} = 0$. Solving these equations, we get the following expressions for the cavitation inception time, $t_c = \widetilde{t}_c\theta$, and the cavitation inception plane, $x_c = \widetilde{x}_c c\theta$ [35]

$$\ln\left[\frac{2(1+\psi)\sinh\widetilde{x}_c}{\widetilde{\sigma}\psi}\right] = \frac{1}{1-\psi}\left[\ln\frac{\psi\cosh\widetilde{x}_c + \sinh\widetilde{x}_c}{\psi^2 - 0.5\widetilde{\sigma}\psi(\psi-1)}\right] - \psi\widetilde{x}_c, \widetilde{t}_c$$
$$= \ln\left[\frac{2(1+\psi)\sinh\widetilde{x}_c}{\widetilde{\sigma}\psi}\right] \tag{27}$$

Hutchinson and Xue [31] proposed that the water layer between the cavitation inception plane and the face plate moves with the face plate as schematically shown in Fig. 12. The mass of the water layer adds to the mass of the face plate, and should be considered in the momentum and the energy calculation of the face plate. Hutchinson and Xue proposed the following empirical expression (28) for the ratio, r_w, of the added mass to the mass of the face plate for sandwich structures with identical front and back face plates and $\widetilde{\sigma} < 0.15$.

$$r_w = 0.71\psi\widetilde{\sigma} \tag{28}$$

The cavitation inception ends stage 1 of the interaction between a shock wave and a sandwich structure. With $\overline{\varepsilon}$ and C, respectively, equaling the average crushing strain and the core thickness, the energy, $\sigma_y\overline{\varepsilon}C$, consumed in crushing the core in stage 2 is found from

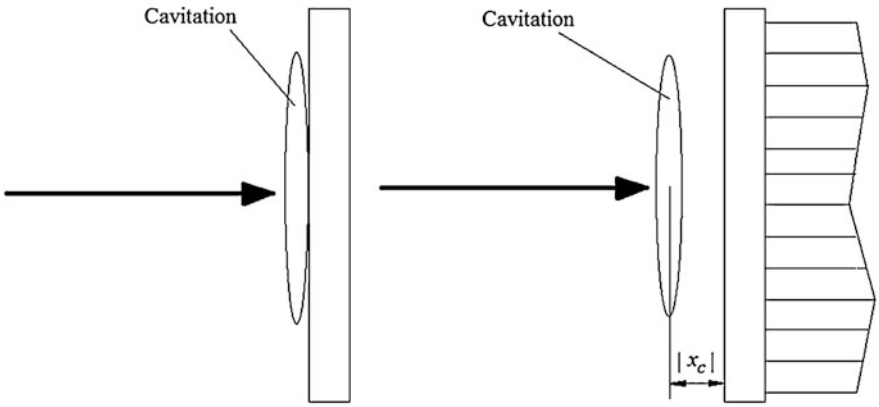

Fig. 12 Schematic representation of the cavitation phenomenon in a blast wave interacting with a (left) monolithic, and (**b**) sandwich plate

$$\sigma_y \bar{\varepsilon} C = \Delta KE = KE_F - KE_I \tag{29}$$

where KE_F (KE_I) is the kinetic energy at the end (beginning) of stage 2. KE_I equals the sum of the kinetic energy of the face plate, added water layer, the core and the back plate. That is,

$$KE_I = \frac{I_f^2}{2(m_w + m_f)} + \frac{I_b^2}{2(m_c + m_f)}, KE_F = \frac{I_t^2}{2(2m_f + m_w + m_c)} \tag{30}$$

In Eq. (30), I_f, I_b and I_t are, respectively, the face plate momentum, combined momentum of the core and the back plate, and the total momentum; m_w, m_c and m_f, respectively, equal the mass of the added water, the core, and the face plate. Furthermore, $I_f = m_f$ multiplied by the face plate velocity at the instant of cavitation. The momentum transferred to the back plate and the core, respectively, equals $\sigma_y t_c$ [31], and $I_t = I_f + I_b$. The stage 2 ends when the face plate, the deformed core and the back plate start moving at the same velocity [17].

In stage 3, the residual kinetic energy causes global bending and shearing off of the face plate. The approximate times of the beginning and the end of the three stages are ([31, 32])

$$t_I = t_c \approx t_0 \frac{\ln \beta}{\beta - 1}, t_{II} \approx \frac{I_T}{2\sigma_y^D}, t_{III} \approx L\sqrt{\rho/\sigma_y} \tag{31}$$

3.3 Bubble Pulsation, Bubble Migration and Cavitation

In addition to a primary shock wave, secondary shocks due to bubble pulsation and bubble migration can significantly damage a ship. As the bubble pulsation occurs after passing of a primary shock, secondary pulses usually affect a different region of the ship due to its motion [7]. The severity of damage due to bubble pulsation is very high when the bubble pulsation frequency is close to a natural frequency of the ship. This bends a ship structure, and the associated damage is called whipping [7]. In severe cases, the peak deflection exceeds the elastic limit causing permanent damage. This is more severe for surface ships than for submarines for which the surrounding water damps resonant vibrations. The damage caused by the bubble migration is significant for explosions occurring under a ship.

Early works in modeling of gas dynamics include those of Gudonov [38, 39] and van Leer [40] who studied one-dimensional (1-D) problems using, respectively, the Lagrangian and the Eulerian schemes with the gas modeled as compressible. An all-purpose computer code, MUSCL (monotonic upstream-centered scheme for conservation laws), was developed to numerically study the phenomenon of gas bubble formation from the explosion [41]. Colella [42] modified the MUSCL

algorithm to formulate gas dynamics in a single Eulerian step instead of a remap from the Lagrangian to the Eulerian coordinates; also see [43]. In subsequent works, the boundary element method (BEM) was extensively used to study the bubble dynamics and the pulsation phenomena. For example, Blake and Gibson [44, 45] and Geers and Hunter [46, 47] studied the growth of a bubble near a free surface and the cavitation near solid boundaries using the BEM.

Bulk cavitation occurs due to the reflection of the incident shock wave off the water surface as a tensile wave. The cavitated zone lies just beneath the water free surface with the upper and the lower boundaries having their centers of curvature at the explosion point. The cavitation envelope collapses after a certain time resulting in water hammer [7] that can produce significant strains in a surface ship positioned close to the bulk cavitation zone. Cavitation also occurs at the fluid-plate interface due to the reflection of the incident pressure pulse from the plate. Due to multiple reflections of this tensile wave between the plate surface and the cavitated zone, several pressure peaks occur at the plate resulting in spray loading [14]. Also, similar to the closing of a cavitation envelope in bulk cavitation, the closing of the hull cavitated region causes water hammer loading on the plate. Although the spray loading magnitude is negligible as compared to the peak pressure, the magnitude of water hammer is significant enough to cause noticeable damage [48].

4 Computational Modeling of Ships Deformations

Early works on mathematical modeling of the FSI include that of Bleich and Sandler [49, 50] who modeled the fluid as bi-linear and studied 1-D wave propagation by using the method of characteristics. Geers [51, 52] has employed the double asymptotic approximation (DAA) based finite element method (FEM) to analyze transient interaction of a flexible structure and an infinite fluid by considering the acoustic media around the structure as a membrane that covers the wet surface of the structure [53]. A major advantage of the DAA is using parameters of the wet surface response to eliminate the need to discretize the media surrounding the structure. Two different DAA based models, characterized according to their computational cost, are presented.

Other significant works on ship-underwater explosion include those of DeRuntz et al. [54] and DeRuntz [55] who developed a numerical package, Underwater Shock Analysis (USA), based on a fluid BEM to model the fluid in a FSI problem that did not capture the cavitation phenomenon and required using an alternative fluid model to prevent the fluid pressure from becoming negative. For example, DeRuntz and Rankin [55] and Fillipa and DeRuntz [56] employed a bilinear fluid model to accomplish this. The computational code, Cavitating Fluid Analyzer (CFA), could treat the cavitation of the fluid. The CFA code is an acoustic fluid formulation based volume element processor which is based on the displacement potential. Shin and Santiago [53] coupled the USA-CFA code with NASTRAN to analyze a 2-D problem, namely deformations of a ship cross-section, and compared results with

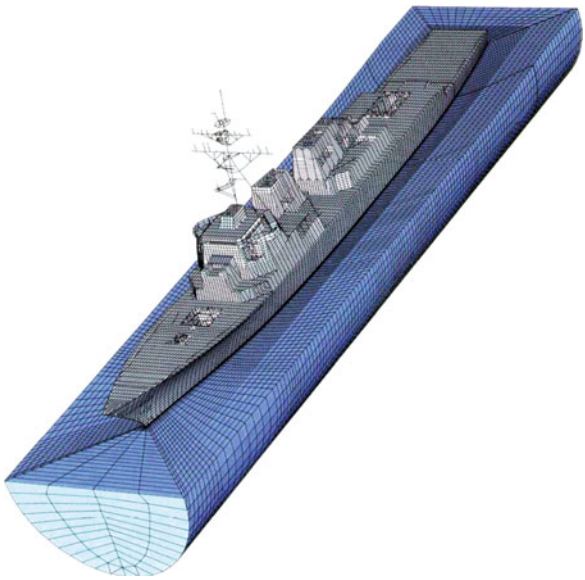

Fig. 13 Discretization of the domain of study into finite elements [58]

and without using the cavitation model, and with and without the DAA. Shin [57] used a coupled LSDYNA-USA code to simulate 3-D deformations of a ship exposed to a blast wave. Solid elements included in LS-DYNA were used to model the ship, and the fluid volume surrounding the ship was modeled using the material type MAT_90 (MAT_ACOUSTIC) that can simulate wave propagation in an irrotational, compressible and either linear or bilinear fluid but not negative pressures in the fluid [55, 57]. Shin's computed results compared well with the ship shock test data. Figure 13 taken from [57] shows the discretization of the domain studied into FEs. Kwon and Cunningham [58] employed the USA-DYNA software to study deformations of a stiffened shell subjected to dynamic impulse loading. Newton simulated the fluid cavitation by using the Cavitation Acoustic Finite Element (CAFE) method [59–62], and compared results with those of Bleich and Sandler [50]. Newton's work was later modified by Felippa and DeRuntz [56]. Rehak et al. [63] also incorporated the cavitation phenomenon in their FSI computational model. The CAFE algorithm used for modeling large scale simulations is resource intensive [64]. Sprague and Geers [65] overcame this by modifying the algorithm and named it the Cavitating Acoustic Spectral Element (CASE) [66, 64]. The CASE and the CAFÉ, respectively, use Legendre polynomials and "trilinear polynomials" as basis functions, and the CASE model uses a non-conformal FE mesh for the FSI modeling.

Klaseboer et al. [66] have compared experimental findings with numerical results for explosions close to a structure by modeling the gas bubble using the BEM and the structure using a nonlinear FE software, PEM-CRASH™. A similar work on the effect of the close proximity blasts on ship like structures was presented in [67]. Huang et al. [68] numerically modeled the FSI problem using ANSYS-AUTODYN. Mair [69] has reviewed other hydrocodes for studying the FSI problems.

4.1 Fluid Structure Interaction of Monolithic Plates

The response of monolithic plates to an underwater explosion has been experimentally analyzed in [66, 70–73], and that due to an air blast wave in [74, 75]. Deformations of a cylindrical shell interacting with a blast wave have been studied in [58, 76]. Taylor [5] proposed a theoretical model of a free standing rigid plate subjected to a pressure pulse and adopted a linear acoustic model of water. He showed that the FSI reduces the momentum transferred to the plate as compared to that for an impact loading on a free standing plate.

The analysis of transient deformations of a plate involves solving the following system of coupled ordinary differential equations generally under null initial conditions [15].

$$[\mathbf{M}]\{\ddot{x}\} + [\mathbf{C}]\{\dot{x}\} + [\mathbf{K}]\{x\} = \{P(t)\}, x(0) = \dot{x}(0) = 0 \tag{32}$$

Here **M**, **C** and **K**, respectively, represent the structural mass, the structural damping and the structural stiffness matrix, and $P(t)$ is the time varying load that can include forces due to the bubble formation, migration, and collapse. The FSI can be accounted for by suitably modifying **M** for the added mass of water. The non-linear compressibility of water was considered in [77–79].

Fleck and Deshpande [17] studied the FSI of a plate by using an exponentially decaying forcing function as employed by Taylor [5]. Using the same forcing function, both linear and nonlinear problems were studied with the FE software ADINA in [80]. Louca et al. [81] compared the response of imperfect and stiffened monolithic plates with the two FE software DYNA3D and ABAQUS/Explicit. Ramajeyathilagam and Vendhan [82] experimentally and numerically (with DYNA3D) studied the deformation and rupture of air-backed clamped rectangular plates. Deformations and tearing of circular plates due to blast loads, studied by Gupta and Nagesh [80] using the FE software ANSYS, were found to correlate well with test observations of [70, 71].

Kwon and Cunningham [58] computationally studied the response of stiffened plates and ring stiffened cylindrical shells by using the coupled BEM and FEM code, USA-DYNA [54, 83] that models the gas bubble and the traveling pressure pulse from the explosion. Hammond and Grzebieta [84] also used USA-DYNA to delineate the structural response of an air backed clamped square plate and found that the computed plate displacements matched well with their own test results but computations under-predicted the plate velocity. They attributed this to ignoring hydrostatic effects of the water volume in the computational model and not having clamped edges in the tests. Flat monolithic plates were tested in [66] using a (4m $\times$ 4m $\times$ 4m) water tank and Detasheet explosives with DP60 detonator, and numerically analyzed with the USA-DYNA code considering the DAA [51, 52] to model the FSI.

4.2 *Fluid Structure Interaction of Composite Plates and Sandwich Panels*

Composite laminates have very high specific modulus and specific strength along the fiber direction than monolithic structures but their response to impact loads is not very encouraging [85] possibly due to several different failure modes. Hall [86] has experimentally studied deformations of glass-reinforced polymer and foam cored sandwich hulls. Mouritz [19, 20] experimentally studied deformations of laminated plates subjected to impulsive loads. Abrate [85] has reviewed the work on impact loading of sandwich structures having laminated face sheets and has discussed their failure mechanisms. Numerical studies [89] of the FSI of a submerged stiffened composite using USA-DYNA code showed that composite plates have better specific energy absorbing characteristics than monolithic plates. The interaction of a composite cylinder with a blast wave was studied theoretically and computationally using ABAQUS in [87]. Fu et al. [26] discussed the fracture resistance properties of impact loaded short glass/carbon fiber reinforced composites.

Hassan and Batra [88–90] developed a mathematical model and a computer code to study the damage initiation and propagation due to fiber breakage, matrix-fiber de-bonding, matrix cracking and de-lamination in AS4/PEEK composites. They approximated the blast wave load [89, 91] as the product of a function of spatial coordinates and a function of time. Values of material parameters in the damage evolution laws were found by using the test data. De Morais et al. [22] experimentally studied the effect of laminate thickness on damage induced under repeated impact loads. Espinosa et al. [27] employed contact/cohesive laws to analyze finite 3-D deformations of glass fiber reinforced polymeric laminates, and compared computed and experimental results. Nezami et al. [92] used the Rayleigh-Ritz method to study the response of a plate under different boundary conditions and subjected to an explosion blast wave. LeBlanc and Shukla [93, 94] highlighted aspects of the matrix-fiber breakage and internal de-lamination on the interaction with low and high energy blast waves of flat and curved glass-epoxy composite panels. Experimental findings were compared with those computed using LS-DYNA, and displayed differences between the two using the Russel error criteria [95].

Sandwich structures are believed to be more efficient than monolithic plates of the same areal density in their interactions with blast waves [35]. Makinen [96] has discussed dissimilarities in the response behavior of a monolithic plate and a sandwich structure by studying in them the cavitation phenomenon using a 1-D model. Deformations of sandwich structures with face and back plates made of monolithic materials have been scrutinized in [17, 30, 31, 33–35] by using the FEM. Liang et al. [32] and McMeeking et al. [97] discussed constitutive properties of prismatic metallic cores, considered effects of the added layer of water between the

cavitation zone and the face plate, and found a good correlation between the numerical results computed with ABAQUS and theoretical results. Librescu and Noiser [98]. and Librescu et al. [99] studied the response of flat composite panels and sandwich plates with anisotropic composite face plates and an orthotropic core to explosive loads. Wei et al. [100] compared test findings on multi-core sandwich structures [101] with those computed using the FE code ABAQUS/Explicit. In [102], the transient response of a submerged cylindrical foam core sandwich panel subjected to shock loading was analyzed using ABAQUS and integrating fluid and structural models. They reported the circumferential strain at different points in the cylinder.

5 Summary of Batra's Team Work

We summarize below some work completed in Batra's group on structural response to extreme loads.

5.1 Homogenization of Material Properties

Gopinath and Batra [103] have recently used three micro-mechanics approaches, namely, the MoCs, the Fourier series analysis and the transformation field analysis, for homogenizing material properties of a unidirectional fiber-reinforced composite with fibers modeled as linearly elastic transversely isotropic and the matrix as a strain-rate dependent elastic-plastic material. They [105] have also characterized the sensitivity of responses from the three approaches with changes in a unit cell configuration. As shown in Fig. 14, the variation of the transverse elastic modulus versus the fiber volume fraction strongly depends upon the homogenization technique employed.

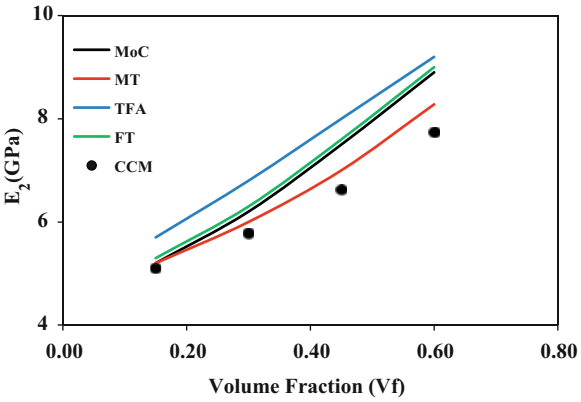

Fig. 14 Variation of the transverse Young's modulus with the fiber volume fraction using different homogenization techniques [103]

5.2 Modeling 3-D Deformations

As stated above, Batra and Hassan [91] identified damage/failure modes (fiber/matrix debonding, fiber breakage, and matrix cracking) with internal variables, used test data to find values of material parameters in their evolution laws, and considered all geometric nonlinearities incorporated in the St. Venant-Kirchhoff material. They postulated a damage surface defined in terms of the transverse normal and the transverse shear tractions at an interface and the interfacial strengths. Delamination ensued once the stress state at an interfacial point reached the damage surface. Subsequently, they introduced two nodes a tiny distance apart at the delamination point and prevented inter-penetration by connecting them with a spring very stiff in compression but weak in tension. They developed in-house a FE based software to analyze large 3-D transient deformations of 4-ply unidirectional fiber-reinforced laminates and delineated the energy dissipated in each failure mode with the blast load modeled as a spatially non-uniformly distributed pressure with the peak value exponentially decaying in time. They simulated damage progression by degrading the stiffness of an FE in which a constituent had failed, and reduced its stiffness to a very small value at complete failure. By retaining such FEs in the analysis, they considered their contributions to inertia forces. The spatial distribution of the matrix cracking and time- histories of the debonding damage at centroids of three different surfaces of the plate are illustrated in Fig. 15.

Whereas Batra and Hassan employed a mechanics of materials approach to homogenize material properties of a unidirectional fiber-reinforced composite, Batra et al. [104] used Aboudi's method of cells (MoCs) with null tangential tractions (e.g., see Robertson and Mall [105]) assumed at an interface between two adjoining cells. Furthermore, they determined stresses in the fiber and the matrix from the macro-level stresses and thus used the constituent level failure criterion but ignored fiber/matrix debonding. They ascertained failed/damaged elements and appropriately reduced their stiffness. The developed UMAT was implemented in ABAQUS. Their computed results for 4 m/s impact deformations of a clamped

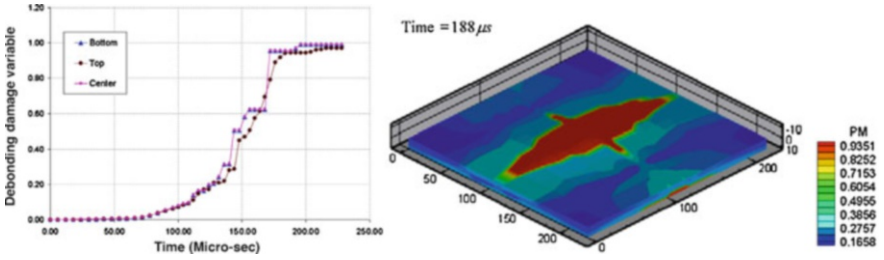

Fig. 15 (Left) Time histories of evolution of the debonding damage variable at centroids of the bottom, the middle and the top surfaces, and (right) fringe plots of the matrix cracking damage variable [91]

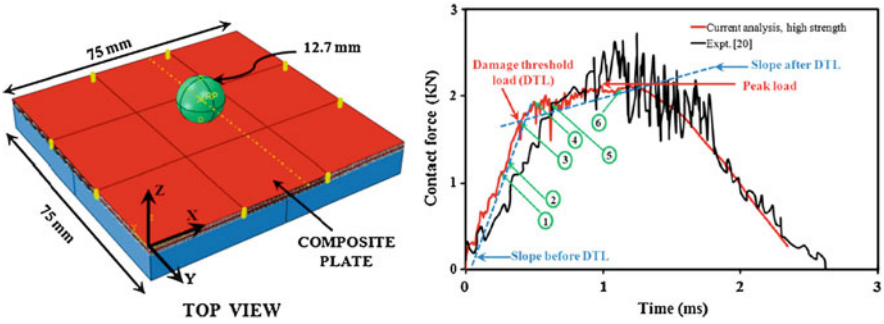

Fig. 16 (Left) Sketch of the impact problem studied with the impactor shown in green, the composite laminate in red, and the supporting steel plate in blue color; (right) contact force time history with points of significance for the damage initiation and propagation [104]

fiber-reinforced laminate qualitatively agreed with the test data. Points 1 through 4 in Fig. 16, respectively, correspond to damage initiation due to fiber compression, matrix tension, fiber tension, and accumulation of the fiber tensile damage.

5.3 *Reduced-Order Models (Third-Order Shear and Normal Deformable Theory)*

We have developed a third-order shear and normal deformable theory (TSNDT) for plates/ shells that accounts for all geometric nonlinearities including the von Karman nonlinearities. The plate material is assumed to be St. Venant-Kirchhoff for which the 2nd Piola-Kirchhoff stress tensor, $\boldsymbol{S}$, is a linear function of the Green-St. Venant strain tensor, $\boldsymbol{E}$. Thus the constitutive relation is objective under superimposed rigid body rotations. Whereas $\boldsymbol{S}$ is work conjugate to $\boldsymbol{E}$ there is no stress tensor that is work conjugate to the von Karman strain tensor. Below we briefly review the TSNDT, and give results for a few problems.

Figure 17 depicts a schematic sketch of a laminated doubly-curved shell composed of N layers of not necessarily equal thickness. Each ply is made of a homogeneous, orthotropic and elastic material with layers perfectly bonded to each other. We denote the total thickness and the constant two principal radii of curvature of the shell by h, R_1 and R_2, respectively. We employ orthogonal curvilinear coordinates (x, y, z) with curves x = constant and y = constant representing principal curvatures on a surface, z = constant. The shell arc lengths in the x and the y directions, respectively, equal a and b with the corresponding platform lengths l_x and l_y. The position vectors of a point p are denoted by $\mathbf{X}$ and $\mathbf{x}$ with respect to the fixed rectangular Cartesian coordinate axes in the reference and the current configuration, respectively, with the X_3- and the x_3-axes parallel to the z-axis.

The components G_{ij} of the metric tensor in the reference configuration are given by

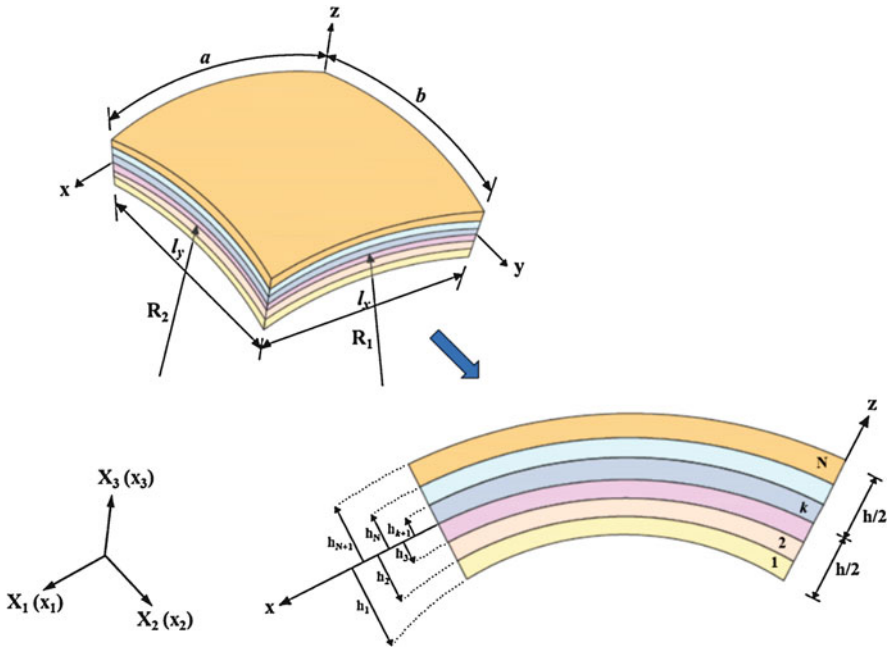

Fig. 17 Geometry and coordinate axes of a doubly-curved N-ply laminated shell

$$G_{ij} = \mathrm{A_i} \cdot \mathrm{A_j}, \mathrm{A_1} = \frac{\partial \mathrm{X}}{\partial x}, \ \mathrm{A_2} = \frac{\partial \mathrm{X}}{\partial y}, \ \mathrm{A_3} = \frac{\partial \mathrm{X}}{\partial z}, \tag{33}$$

where $\mathrm{A_i} \cdot \mathrm{A_j}$ equals the inner product between vectors $\mathrm{A_i}$ and $\mathrm{A_j}$. For orthogonal curvilinear coordinate system, G_{ij} is non-zero only when i = j. We define $\overline{e}_i = \frac{\mathbf{A}_{(i)}}{\mathrm{H}_{(i)}}$ (no sum on i), where $\mathrm{H}_1 = \left(1 + \frac{z}{\mathrm{R}_1}\right), \ \mathrm{H}_2 = \left(1 + \frac{z}{\mathrm{R}_2}\right), \ \mathrm{H}_3 = 1$. For the TSNDT the displacement, $\boldsymbol{u} = \boldsymbol{x} - \boldsymbol{X}$ or (u, v, w), of a point in the shell is expressed as

$$\mathbf{d} = \mathbf{d}_t + \mathbf{Z}_\theta \mathbf{d}_\theta + \mathbf{Z}_\phi \mathbf{d}_\phi + \mathbf{Z}_\gamma \mathbf{d}_\gamma \tag{34}$$

where

$$\begin{aligned}
&\mathbf{d} = [\mathrm{u} \ \ \mathrm{v} \ \ \mathrm{w}]^{\mathrm{T}}, \mathrm{d_t} = [\mathrm{u_0} \quad \mathrm{v_0} \quad \mathrm{w_0}]^{\mathrm{T}}, \\
&\mathrm{d_\theta} = [\theta_\mathrm{x} \ \ \theta_\mathrm{y} \ \ \theta_\mathrm{z}]^{\mathrm{T}}, \ \mathrm{d_\phi} = [\phi_\mathrm{x} \ \ \phi_\mathrm{y} \ \ \phi_\mathrm{z}]^{\mathrm{T}}, \ \mathrm{d_\gamma} = [\gamma_\mathrm{x} \ \ \gamma_\mathrm{y} \ \ \gamma_\mathrm{z}]^{\mathrm{T}}, \\
&\mathrm{u_0} = \mathrm{u(x, y, 0, t)}, \quad \mathrm{v_0} = \mathrm{v(x, y, 0, t)}, \quad \mathrm{w_0} = \mathrm{w(x, y, 0, t)}, \\
&\mathrm{Z_\theta} = \mathrm{zI}, \mathrm{Z_\phi} = \mathrm{z^2 I}, \mathrm{Z_\gamma} = \mathrm{z^3 I}, \mathrm{I \text{ is the identity matrix}}
\end{aligned}$$

We first find physical components of the displacement gradient, $\boldsymbol{F}$, and then find $\boldsymbol{E} = \frac{1}{2}\left(\boldsymbol{F}^T\boldsymbol{F} - \mathbf{1}\right)$. We assume that the material of each layer is St. Venant-Kirchhoff

for which the strain energy density, W, per unit reference volume, and the relation between $\boldsymbol{S}$ and $\boldsymbol{E}$ are

$$W = \frac{1}{2} E_{mn} C_{mn\alpha\beta} E_{\alpha\beta}, C_{mn\alpha\beta} = C_{\alpha\beta mn} = C_{nm\alpha\beta}, S_{mn} = \frac{\partial W}{\partial E_{mn}}. \tag{35}$$

Here $\boldsymbol{C}$ is the fourth-order elasticity tensor having 21, 9, 5 and 2 independent components for a general anisotropic, orthotropic, transversely isotropic and isotropic material, respectively. The strain energy density for the St. Venant-Kirchhoff material reduces to that of a Hookean material if the finite strain tensor $\boldsymbol{E}$ is replaced by the infinitesimal deformations strain tensor.

5.3.1 Effect of Curvature on Deformations of Shells

We use the linear theory valid for infinitesimal deformations to study transient deformations of four clamped spherical sandwich shells of equal principal radii given by R/$a = \infty$ (plate), 5, 1 and 0.5. Each shell is comprised of a soft honeycomb core modeled as an isotropic material with the top and the bottom face sheets made of an orthotropic material with fibers oriented at 45° with respect to the x-axis. The total thickness of the shell, h = 22 mm, and thicknesses of the core and each face sheet are 16 mm and 3 mm, respectively. Furthermore, the aspect ratio of the shell, a/h = 10 and $a = b$. Values of face sheets material parameters are

$E_1 = 251$ GPa, $E_2 = 48$ GPa, $E_3 = 7.5$ GPa, $G_{12} = 13.6$ GPa, $G_{13} = 12$ GPa, $G_{23} = 4.7$ GPa,

$\nu_{12} = 0.036$, $\nu_{13} = 0.25$, $\nu_{23} = 0.171$, $\rho = 1600$ kg/m^3

and those of the core isotropic material are, Young's modulus $E = E_1/100$ and Poisson's ratio $\nu = 0.2$.

In Table 2 we have listed the first ten lowest natural frequencies of free vibration and the maximum natural frequency of the four shells. These values suggest that each frequency increases with a decrease in R, and the fundamental mode frequency of the shell with R/$a = 1$ is nearly twice of that of the corresponding flat plate.

In Fig. 18 we have depicted time histories of the deflection of the core centroid, w ($a/2, b/2, 0$), for the four shells having traction free bottom surface and the top surface subjected to the pressure due to an explosive load given by

$$P(r,t) = \left(-0.0005r^4 + 0.01r^3 - 0.0586r^2 - 0.001r + 1\right)P(t) \tag{36}$$

where r is the distance in cm, from the shell top surface center, and

Table 2 Natural frequencies (Hz) of four sandwich shells [106]

Mode	Plate	R/$a = 5$	R/$a = 1$	R/$a = 0.5$
1	3,644	3,960	7,022	8,450
2	5,826	6,093	7,383	9,889
3	6,305	6,525	8,331	10,553
4	7,946	8,281	9,475	10,630
5	8,966	9,305	10,068	12,517
6	9,214	9,632	10,450	12,986
7	10,234	10,647	11,602	13,286
8	10,981	11,533	11,660	13,736
9	11,850	11,857	12,193	14,665
10	12,252	12,860	12,560	15,524
Maximum frequency	643,872	822,912	658,275	685,535

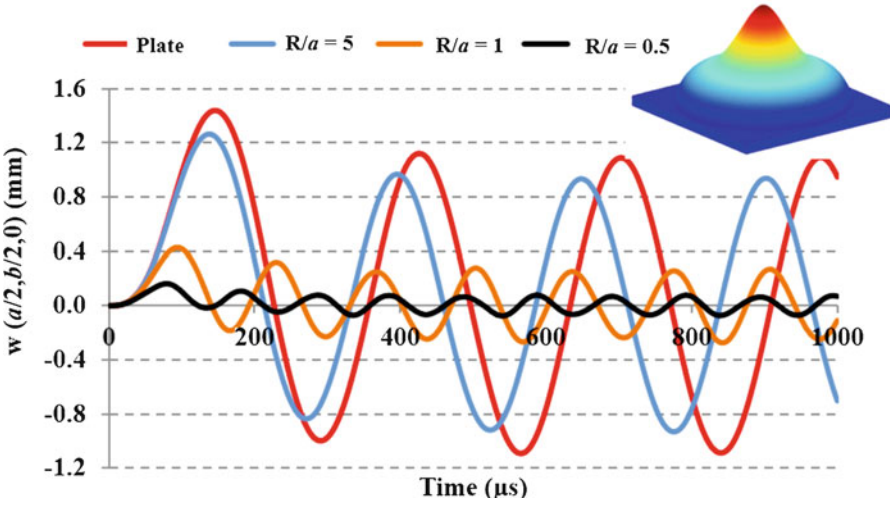

Fig. 18 Time histories of the deflection of centroid of the core for the four sandwich shells with R/$a = \infty$ (plate), R/$a = 5$, R/$a = 1$ and R/$a = 0.5$ [106]

$$P(t) = \begin{cases} 10t/60 \quad \text{MPa}, & t \leq 60\ \mu\text{s} \\ 10e^{-\frac{(t-60)}{30}} \quad \text{MPa}, & t > 60\ \mu\text{s} \end{cases} \tag{37}$$

The spatial distribution of the load is depicted in Fig. 18 inset. A comparison of these histories reveals that the maximum deflection decreases with an increase in the shell curvature. We note that the pressure applied at every point on the top surface linearly increases for the first 60 μs and then exponentially decreases becoming essentially zero for t > 120 μs. Thus for t > 120 μs, the shells freely vibrate.

In Fig. 19 we have displayed time histories of the axial stress, $\sigma_x(a/2, b/2, z)$, at centroids of each face sheet and the core for the shell with R/$a = 5$. Similar results for

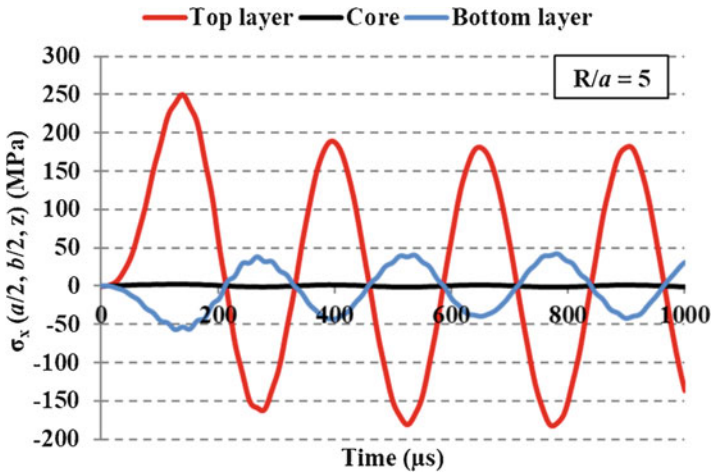

Fig. 19 Time histories of the axial stress, at centroid of each layer for the sandwich shell with R/$a = 5$ [106]

the other three shells suggest that, except for the flat plate, the maximum magnitude of the bending stress in the shell decreases with a decrease in the value of R or an increase in the shell curvature.

5.3.2 Effect of Geometric Nonlinearities on Orthotropic Plate's Deformations

For the transient pressure, given by Eq. (36) with the right-hand side of Eq. (37) replaced by $P_0 e^{-(t-t_r)/\theta}$, $P_0 = 1\ GPa$, θ given by Eq. (1c), applied to the top surface of a clamped 22 cm × 22 cm plate made of a homogeneous and orthotropic material, we compare in Fig. 20 the centroidal deflection and the Cauchy stress σ_{11} at (a/2, b/2, h/2) time histories predicted by the linear and the nonlinear theories. Both the maximum deflection and the maximum value of σ_{11} from the nonlinear theory are considerably less than those from the linear theory. The linear theory over-predicts the peak displacement by a factor of almost 2, and the peak Cauchy stress by a factor of 2.5. However, this is not always the case as illustrated by results for the full sine wave beam studied in [107].

5.3.3 Stacking Sequence Optimization for Maximizing the Failure Initiation Load [108]

The objective is to find the fiber orientation angle in each ply of a rectangular laminate subjected to transverse loads on its top surface that maximizes the first failure load using the Tsai-Wu failure criterion, and for this stacking sequence find the ultimate failure load. We have numerically solved the problem by using the Nest-Site Selection (NeSS)

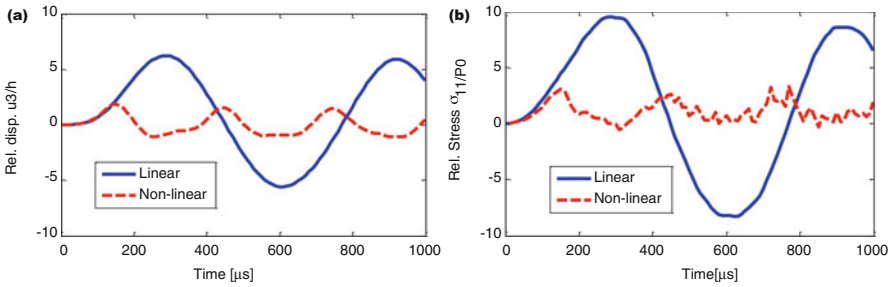

Fig. 20 Comparison of the (**a**) out of plane displacement of the plate centroid, and (**b**) σ_{11} at the centroid of the top face from the linear and the nonlinear theories [106]

optimization algorithm, the TSNDT, the FEM, and a one-step stress-recovery scheme (SRS), and shown that the computed six stress components have values close to those given by the solution of the 3-D linear elasticity equations with the FE software, ABAQUS. The number of layers and the thickness of each layer are kept fixed. The failure index, F, of the Tsai-Wu criterion is calculated at 36,000 points in the structure using stress components with respect to the material principal axes. For the first failure load to have the highest value, the fiber orientations in each ply should be such that the maximum value, F_{max}, of F for the structure has the least value. Subsequent to the initiation of the failure at a point and the degradation of material properties there, the structure becomes nonhomogeneous. The optimization problem is stated as follows.

$$\text{Find } \boldsymbol{\theta} = \{\theta_1, \theta_2, \theta_3, \ldots, \theta_n\},\ \theta_i \in [-90^{\circ}, 90^{\circ}] \text{ in } 1^{\circ} \text{ increment for } i = 1, \ldots, n,$$

$$\text{so that } F_{\max} = \sup\{F(X_1, X_2, X_3), (X_1, X_2, X_3) \in \Omega = [0, a] \times [0, b] \times [-\frac{h}{2}, \frac{h}{2}]\}$$

has the least value. Here θ_i is the fiber orientation angle in the *ith* ply measured counter clockwise from the positive X_1-axis, and n equals the number of plies. Subsequent to ascertaining the optimal stacking sequence, we perform progressive failure analysis to find the ultimate failure load.

We analyze below the optimization problem for a 10-layer square laminate of side $a = 22$ cm, $a/h = 10$, the load distribution illustrated in Fig. 18 inset, and values of material parameters listed in Table 3.

In Table 4 we have listed the five optimal stacking sequences (corresponding to five randomly chosen values of the initial stacking sequence) for the pressure load given by Eq. (32) the first failure load L_F (or q_0) and the ultimate failure load L_U. The (L_F, L_U) for the $[0]_{10}$, $[0/90]_5$ and $[0_5/90_5]$ clamped laminates, respectively, are (12.41, 20.99), (14.67, 24.48) and (7.22, 10.28). For the three loadings studied, the $[0/90]_5$ laminate has the maximum L_U. Values in the column "% increase" are the relative difference between L_F and L_U. Laminates with non-traditional fiber orientations have higher L_F and L_U than those with commonly used fiber angles.

We note that (a) for a simply supported laminate, L_U and L_F are essentially equal to each other, (b) the L_U for a clamped plate is 32% more than that for a simply supported laminate, (c) for clamped laminates the ratio, L_U/L_F, varies from 1.4 to 1.2 and depends upon the stacking sequence and the load type, and (d) the stacking sequence for the maximum L_F need not have the maximum L_U.

Table 3 Values of material parameters for a lamina with respect to material principal axes

Elastic moduli (GPa)			Shear moduli (GPa)			Poisson's ratios		
E_1	E_2	E_3	G_{12}	G_{13}	G_{23}	ν_{12}	ν_{13}	ν_{23}
132.5	10.8	10.8	5.7	5.7	3.4	0.24	0.24	0.49
Strength parameters (MPa)								
X_T	X_C	Y_T	Y_C	Z_T	Z_C	R	S	T
1515	1697	43.8	43.8	43.8	43.8	67.6	86.9	86.9

Table 4 Optimal designs of plates for two boundary conditions with the fiber orientation angle measured counter-clockwise from the X_1-axis entries below should not be bold.

Boundary conditions	Design	Stacking sequence	First failure load (MPa)	Ultimate failure load (MPa)	% increase
Clamped	c1	[−46/43/29/79/−29/−13/−54/−79/−27/49]	20.15	25.08	24.48
	c2	[−48/27/31/−44/−32/−71/−13/3/74/−37]	20.07	23.18	15.48
	c3	[50/−24/−61/31/39/43/55/83/−49/44]	20.18	22.85	13.25
	c4	[−52/26/47/−39/−30/−22/−62/−68/−66/44]	19.54	22.63	15.81
	c5	[−50/31/68/−62/−43/−67/−12/−79/63/−46]	20.06	22.45	11.92
Simply supported	c1'	[29/−35/−37/13/−32/6/45/35/47/−32]	18.96	18.96	0
	c2'	[−63/46/40/−84/77/−81/−60/43/−44/56]	18.40	18.40	0
	c3'	[−32/52/83/76/81/21/42/−45/−45/61]	18.31	18.31	0
	c4'	[−24/29/46/16/−14/48/−17/−14/−43/33]	18.02	18.02	0
	c5'	[25/−36/30/−52/15/87/19/45/50/−26]	17.59	17.59	0

For the two boundary conditions, we have exhibited in Fig. 21 the final plate configurations with the failed material separately shown. The plate thickness has been enlarged by a factor of 12 and various layers are differently colored for ease of viewing. For a simply supported laminate, the failure initiates at the centroid of either the top or the bottom surface and rapidly propagates radially outwards and along the plate thickness creating a virtual hole (because elements in our work are not really deleted but are made very weak). The laminate ultimately fails at a load very close to the first failure load. For the clamped plate, the failure initiates at points near the edges and propagates downwards along the thickness. Some material near the plate vertical centroidal axis also has failed prior to the application of the ultimate load.

In Fig. 22, we have displayed the fraction of failed points and the maximum vertical deflection (with their scales shown on the left and the right vertical axes,

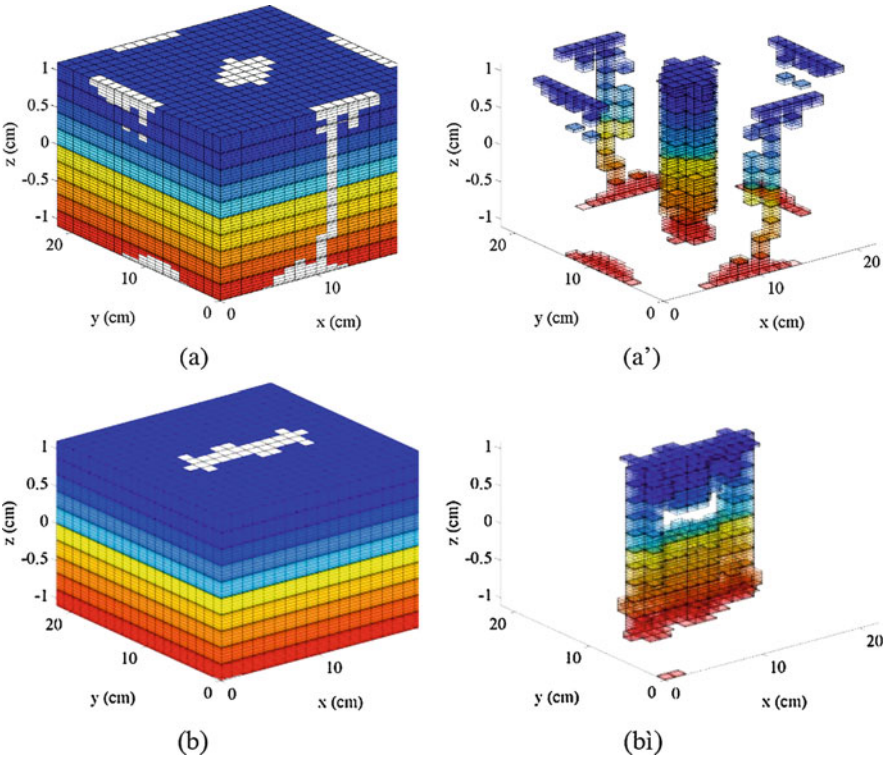

Fig. 21 The final laminate configurations for (**a**) clamped plate c1 and (**b**) simply supported plate c1' with only the failed material depicted in Figs. (**a'**) and (**b'**) [108]

respectively) versus the peak load for the clamped plates under (a) uniform, (b) sinusoidal, and (c) non-uniform distributed load given by Eq. (36) with P(t) = 1 applied on the top surface. Taking the rate of increase of the fraction of failed points as an indicator of the rate of progression of failure in the laminate, it is evident that the failure/damage propagates most (least) rapidly for the uniformly (non-uniformly) distributed load.

5.3.4 Fluid-Structure Interaction

Qin and Batra [109] developed a hydroelastic model using a {3, 2} sandwich plate theory (i.e., deformations of face sheets are simulated using the Kirchhoff plate theory and for the core in-plane and transverse displacements are, respectively, polynomials of degree 3 and 2 in the z-coordinate) and Wagner's water impact theory to study a slamming process. They found that considering wedge's deformations significantly affects the slamming pressure between the water and the wedge.

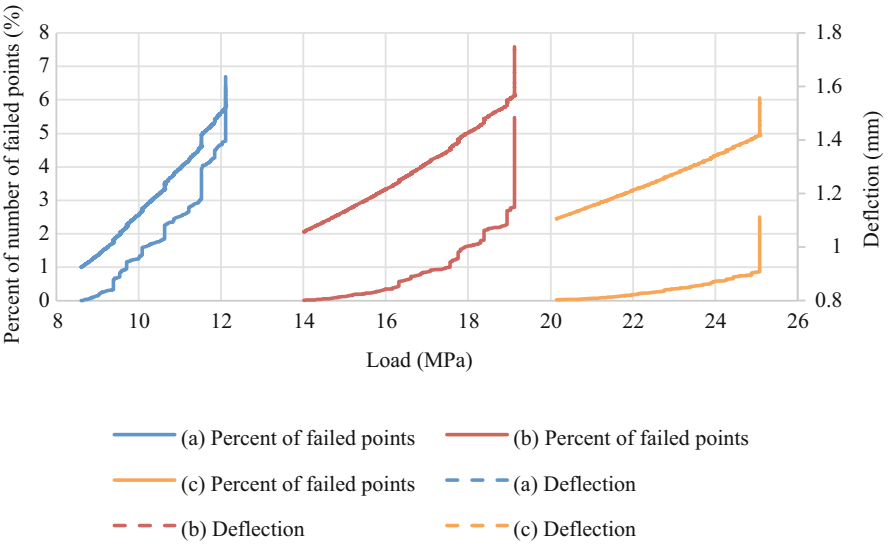

Fig. 22 The variation of the percentage of the number of failed points and the maximum vertical deflection with the peak load for the clamped plates subjected to (**a**) uniform normal traction, (**b**) sinusoidal traction, and (**c**) non-uniform traction [108]

Das and Batra [110] used the FE commercial software, LSDYNA, and the coupled Lagrangian and Eulerian (sometimes called ALE) approach to describe finite plane strain deformations of a hull panel. A linear relation between the Cauchy stress tensor and the Almansi-Hamel strain tensor was employed for the hull material and the water was modeled as an inviscid compressible fluid. The continuity of surface tractions and the inter-penetration of water into the hull was satisfied by using a penalty method. They delineated jet flows near the edges of a wetted hull, and analyzed delamination induced in a sandwich composite panel. As displayed in Fig. 23, the slamming pressure can be considered as a wave traveling along the hull with peak value gradually decreasing as the wave propagates along the hull.

Xiao and Batra [111] analyzed finite plane strain elastic deformation of a sandwich panel by using a layer wise TSNDT. They numerically solved the irrotational and isochoric flow equations by the BEM and nonlinear governing equations of the solid by the FEM. They employed a cohesive zone model to decipher mixed mode delamination at an interface between a face sheet and the core, and delineated effects of hull curvature on the hydroelastic interaction. Figure 24 depicts time-histories of a panel centroid deflection with and without considering delamination. For one of the problems studied, the energy dissipated during delamination was quantified as 8% of the total work done on the hull.

For water slamming problems studied above, the solid body need not be immersed in the fluid. Qu and Batra [112] developed a numerical algorithm for studying the interaction of inviscid and compressible flows with arbitrary shaped moving rigid solids in which the fluid flow equations are solved on a fixed

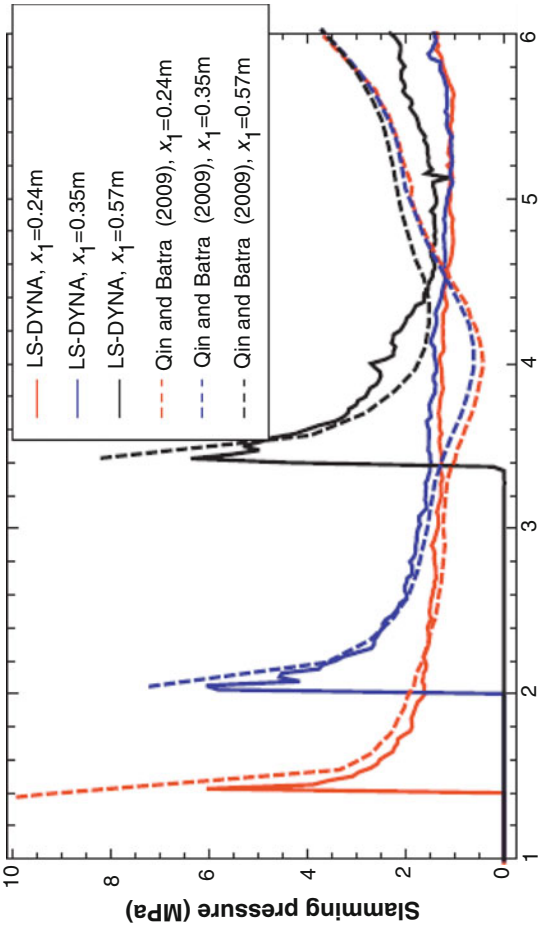

Fig. 23 Time histories of the interface pressure at 3 locations on the hull-water interface [110]

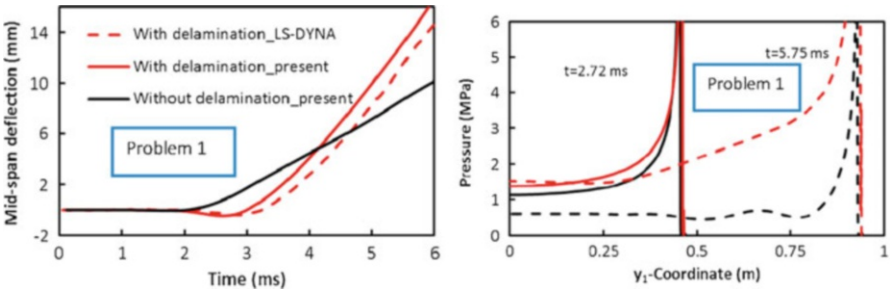

Fig. 24 Time histories of the deflection of a straight panel centroid, and the hydroelastic pressure distribution at two different times [111]

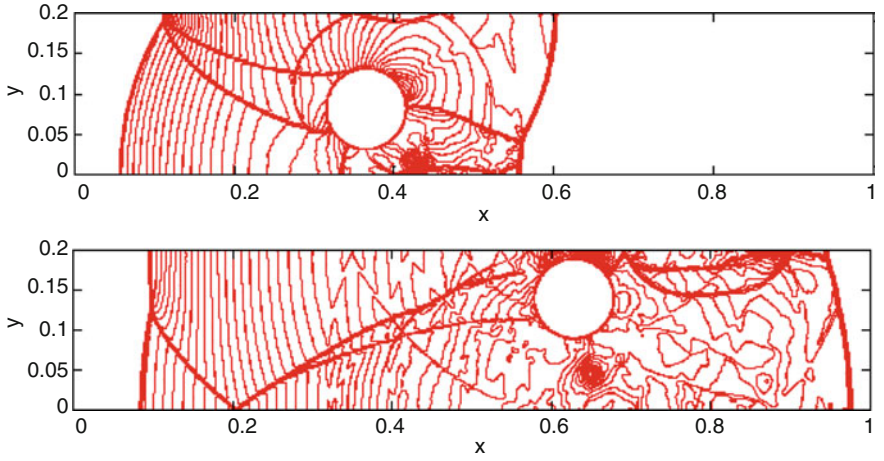

Fig. 25 Pressure contours at (top) t = 0.140 s and (bottom) t = 0.255 s (50 contours from 0 to 22) [112]

rectangular Cartesian grid using a 5th order weighted essentially non-oscillatory (WENO) scheme. The continuity of pressure at the interface was enforced with a constrained moving least-squares sharp interface method and the continuity of normal velocities by a penalty method. The solution is advanced in time by alternately using the 3rd order Runge-Kutta and the implicit Newmark integration schemes for the fluid and the solid motion equations. They studied the lift-off of a 0.1 m diameter rigid circular cylinder of mass density 7.6 kg/m^3 initially resting at (0.15 m, 0.05 m) on the lower wall of an air filled channel. The cylinder is driven by an incident shock wave with Mach number = 3 starting at 0.08 m; e.g. see [113, 114]. The instantaneous pressure contours at two times exhibited in Fig. 25 reveal the existence of a strong vortex below the cylinder that is probably associated with a Kelvin-Helmholtz instability of the contact discontinuity.

Qu et al. [115] have extended the work in [112] and [113] to high speed compressible viscous flows modeled by the Navier-Stokes equations that are discretized using a low-diffusion flux splitting method for the inviscid fluxes and

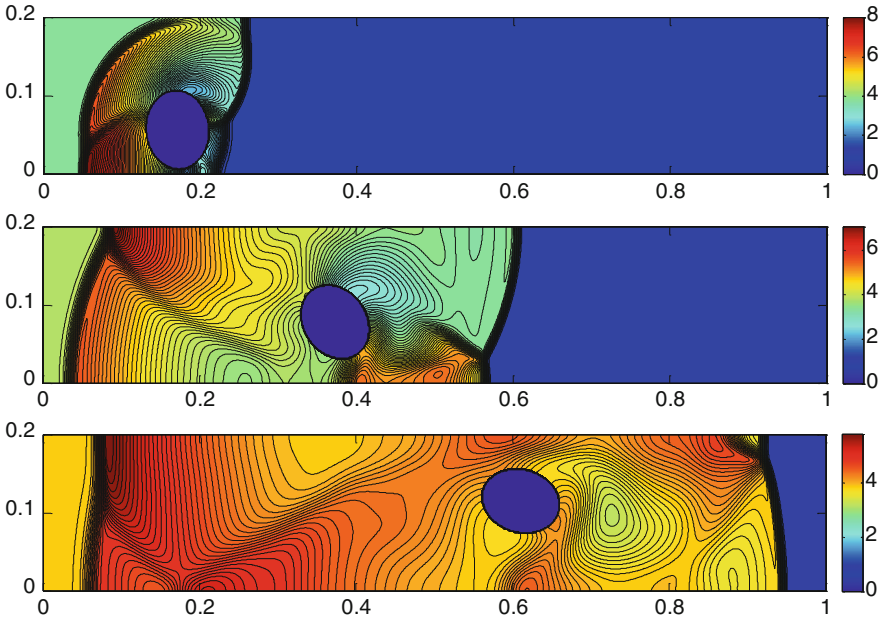

Fig. 26 Contours of mass density from top to bottom: t = 0.05 (100 contours from 0 to 8.11), t = 0.15 (100 contours from 0 to 7.12), and t = 0.25 (100 contours from 0 to 5.83) [115]

conservative higher-order central differences for the viscous components. Referring the reader to [115] for details, we have exhibited in Fig. 26 the instantaneous pressure contours for the problem of the lifting off of an elliptic cylinder.

6 Conclusions

We have shown that a third-order shear and normal deformable plate/shell theory coupled with a one-step stress recovery scheme provides reasonably accurate values of the three displacement components and the six stress components. The blast/explosion load has been approximated as the product of a function of time and a function of the spatial coordinates. The optimal stacking sequence for a laminate that maximizes the first failure load has plies with fiber angles quite different from those commonly studied, and do not conform to a functionally graded laminate. The analyses of water slamming problems suggest that the pressure on the hull surface, modeled as a wedge, can be regarded as a traveling pressure wave with the peak value decaying as it travels away from the keel. The hull curvature and the hydroelastic interaction strongly influence the pressure wave. The developed sharp-interface immersed boundary method for numerically studying the interaction between high speed viscous flows and rigid solids can be extended to deformable solids.

Acknowledgments The work was supported by the Office of Naval Research grant, N000141812548, to Virginia Polytechnic Institute and State University. Views expressed in this paper are those of the authors and neither of their organizations nor of the ONR.

References

1. Cullis I (2001) Blast waves and how they interact with structures. J R Army Med Corps 147 (1):16–26
2. Keil A (1961) The response of ships to underwater explosions. David Taylor Model Basin, Washington
3. Rayleigh L (1917) VIII. On the pressure developed in a liquid during the collapse of a spherical cavity. Lond Edinb Dubl Phil Mag & J Sci 34(200):94–98
4. Cole RH, Weller R (1948) Underwater explosions. Phys Today 1:35
5. Taylor G (1963) The pressure and impulse of submarine explosion waves on plates, The scientific papers of GI Taylor 3:287–303
6. Rajendran R, Narasimhan K (2006) Deformation and fracture behaviour of plate specimens subjected to underwater explosion—a review. Int J Impact Eng 32(12):1945–1963
7. Reid W (1996) The response of surface ships to underwater explosions, department of defence. Defence Science and Technology Organisation, Melbourne
8. Shin Y (1996) Naval ship shock and design analysis. Course notes for underwater shock analysis, Naval Postgraduate School, Monterey 87
9. Snay HG (1957) Hydrodynamics of underwater explosions. In symposium on naval hydrodynamics
10. Costanzo FA, Gordon JD (1980) An analysis of bulk cavitation in deep water, DTNSRDC, UERD Report
11. Nurick G, Martin J (1989) Deformation of thin plates subjected to impulsive loading—a review Part 1: Theoretical considerations. Int J Impact Eng 8(2):159–170
12. Nurick G, Martin J (1989) Deformation of thin plates subjected to impulsive loading—a review part II: experimental studies. Int J Impact Eng 8(2):171–186
13. Wierzbicki T, Nurick G (1996) Large deformation of thin plates under localised impulsive loading. Int J Impact Eng 18(7–8):899–918
14. Rajendran R, Narasimhan K (2001) Damage prediction of clamped circular plates subjected to contact underwater explosion. Int J Impact Eng 25(4):373–386
15. Rajendran R, Lee J (2009) Blast loaded plates. Mar Struct 22(2):99–127
16. Kennard E (1994) The effect of a pressure wave on a plate or a diaphragm. David Taylor Model Basin, Washington
17. Fleck N, Deshpande V (2004) The resistance of clamped sandwich beams to shock loading. J Appl Mech 71(3):386–401
18. Liu Z, Young YL (2008) Transient response of submerged plates subject to underwater shock loading: an analytical perspective. J Appl Mech 75(4):044504
19. Mouritz A (1995) The damage to stitched GRP laminates by underwater explosion shock loading. Compos Sci Technol 55(4):365–374
20. Mouritz A (1996) The effect of underwater explosion shock loading on the flexural properties of GRP laminates. Int J Impact Eng 18(2):129–139
21. Wen H (2001) Penetration and perforation of thick FRP laminates. Compos Sci Technol 61 (8):1163–1172
22. De Morais W, Monteiro S, d'Almeida J (2005) Effect of the laminate thickness on the composite strength to repeated low energy impacts. Compos Struct 70(2):223–228

23. Gellert E, Cimpoeru S, Woodward R (2000) A study of the effect of target thickness on the ballistic perforation of glass-fibre-reinforced plastic composites. Int J Impact Eng 24 (5):445–456
24. Sierakowski RL, Chaturvedi SK (1997) Dynamic loading and characterization of fiber-reinforced composites, dynamic loading and characterization of fiber-reinforced composites, by Robert L, Sierakowski, Shive K, Chaturvedi, pp. 252. ISBN 0-471-13824-X. Wiley-VCH: pp 252
25. Sjögren B (2001) Static strength of CFRP laminates with embedded fiber-optic edge connectors. Compos Part A Appl Sci Manuf 32(2):189–196
26. Fu S, Lauke B, Mäder E, Hu X, Yue C (1999) Fracture resistance of short-glass-fiber-reinforced and short-carbon-fiber-reinforced polypropylene under charpy impact load and its dependence on processing. J Mater Process Tech 89:501–507
27. Espinosa H, Dwivedi S, Lu HC (2000) Modeling impact induced delamination of woven fiber reinforced composites with contact/cohesive laws. Comput Methods Appl Mech Eng 183 (3–4):259–290
28. Roy R, Sarkar B, Bose N (2001) Impact fatigue of glass fibre–vinylester resin composites. Compos Part A Appl Sci Manuf 32(6):871–876
29. Mouritz AP, Gellert E, Burchill P, Challis K (2001) Review of advanced composite structures for naval ships and submarines. Compos Struct 53(1):21–42
30. Xue Z, Hutchinson JW (2004) A comparative study of impulse-resistant metal sandwich plates. Int J Impact Eng 30(10):1283–1305
31. Hutchinson JW, Xue Z (2005) Metal sandwich plates optimized for pressure impulses. Int J Mech Sci 47(4–5):545–569
32. Liang Y, Spuskanyuk AV, Flores SE, Hayhurst DR, Hutchinson JW, McMeeking RM, Evans AG (2007) The response of metallic sandwich panels to water blast. J Appl Mech 74(1):81–99
33. Xue Z, Hutchinson JW (2003) Preliminary assessment of sandwich plates subject to blast loads. Int J Mech Sci 45(4):687–705
34. Xue Z, Hutchinson JW (2006) Crush dynamics of square honeycomb sandwich cores. Int J Numer Methods Eng 65(13):2221–2245
35. Deshpande V, Fleck N (2005) One-dimensional response of sandwich plates to underwater shock loading. J Mech Phys Solids 53(11):2347–2383
36. Qiu X, Deshpande V, Fleck N (2003) Finite element analysis of the dynamic response of clamped sandwich beams subject to shock loading. Eur J Mech A-Solid 22(6):801–814
37. Rabczuk T, Samaniego E, Belytschko T (2007) Simplified model for predicting impulsive loads on submerged structures to account for fluid-structure interaction. Int J Impact Eng 34 (2):163–177
38. Godunov SK (1959) A difference method for numerical calculation of discontinuous solutions of the equations of hydrodynamics. Mat Sb 89(3):271–306
39. Godunov SK, Zabrodin AV, Prokopov GP (1962) A computational scheme for two-dimensional non stationary problems of gas dynamics and calculation of the flow from a shock wave approaching a stationary state. USSR Comput Math & Math Phys 1 (4):1187–1219
40. Van Leer B (1979) Towards the ultimate conservative difference scheme. V. A second-order sequel to Godunov's method. J Comput Phys 32(1):101–136
41. Van Leer B, Woodward P (1979) The MUSCL code for compressible flow: philosophy and results. TICOM conference
42. Colella P (1985) A direct Eulerian MUSCL scheme for gas dynamics. SIAM J Sci Comput 6 (1):104–117
43. Wardlaw AB, Mair HU (1998) Spherical solutions of an underwater explosion bubble. Shock Vib 5(2):89–102
44. Blake JR, Gibson D (1981) Growth and collapse of a vapour cavity near a free surface. J Fluid Mech 111:123–140

45. Blake JR, Gibson D (1987) Cavitation bubbles near boundaries. Annu Rev Fluid Mech 19 (1):99–123
46. Geers TL, Hunter KS (2002) An integrated wave-effects model for an underwater explosion bubble. J Acoust Soc Am 111(4):1584–1601
47. Hunter KS, Geers TL (2004) Pressure and velocity fields produced by an underwater explosion. J Acoust Soc Am 115(4):1483–1496
48. Rajendran R, Satyanarayana K (1997) Interaction of finite amplitude acoustic waves with a plane plate. JASI 25:V5
49. Bleich H, Sandler IS (1968) Dynamic interaction between structures and bilinear fluids. Columbia University, New York
50. Bleich H, Sandler I (1970) Interaction between structures and bilinear fluids. Int J Solid Struct 6(5):617–639
51. Geers TL (1971) Residual potential and approximate methods for three-dimensional fluid-structure interaction problems. J Acoust Soc Am 49(5B):1505–1510
52. Geers TL (1978) Doubly asymptotic approximations for transient motions of submerged structures. J Acoust Soc Am 64(5):1500–1508
53. Shin YS, Santiago LD (1998) Surface ship shock modeling and simulation: two-dimensional analysis. Shock Vib 5(2):129–137
54. DeRuntz J, Geers T, Felippa C (1980) The underwater shock analysis code (USA-version 3): a reference manual. Lockheed Missiles and Space Co Inc, Palo Alto
55. DeRuntz Jr, JA, Rankin C (1989) Applications of the USA-STAGS-CFA code to nonlinear fluid-structure interaction problems in underwater shock of submerged structures, In Proceedings of the 60th shock and vibration symposium
56. Felippa C, DeRuntz J (1984) Finite element analysis of shock-induced hull cavitation. Comput Methods Appl Mech Eng 44(3):297–337
57. Shin YS (2004) Ship shock modeling and simulation for far-field underwater explosion. Comput Struct 82(23–26):2211–2219
58. Kwon Y, Cunningham R (1998) Comparison of USA-DYNA finite element models for a stiffened shell subject to underwater shock. Comput Struct 66(1):127–144
59. Newton R (1978) Effects of cavitation on underwater shock loading—axisymmetric geometry, technical ReportNPS-69-78-017PR. Naval Postgraduate School, Monterey
60. Newton RE (1978) Effects of cavitation on underwater shock loading. Part 1. Naval Postgraduate School, Monterey
61. Newton R (1980) Finite element analysis of shock-induced cavitation. ASCE Spring Convention, Portland
62. Newton RE (1981) Effects of cavitation on underwater shock loading-plane problem. Naval Postgraduate School, Monterey
63. Rehak ML, DiMaggio FL, Sandler IS (1985) Interactive approximations for a cavitating fluid around a floating structure. Comput Struct 21(6):1159–1175
64. Shin YS, Schneider NA (2003) Ship shock trial simulation of USS Winston S. Churchill (DDG 81): modeling and simulation strategy and surrounding fluid volume effects, Shock and vibration symposium
65. Sprague M, Geers T (2004) A spectral-element method for modelling cavitation in transient fluid–structure interaction. Int J Numer Methods Eng 60(15):2467–2499
66. Klaseboer E, Hung K, Wang C, Wang C, Khoo B, Boyce P, Debono S, Charlier H (2005) Experimental and numerical investigation of the dynamics of an underwater explosion bubble near a resilient/rigid structure. J Fluid Mech 537:387–413
67. Webster KG (2007) Investigation of close proximity underwater explosion effects on a ship-like structure using the multi-material arbitrary lagrangian eulerian finite element method, Virginia Tech
68. Huang H, Jiao QJ, Nie JX, Qin JF (2011) Numerical modeling of underwater explosion by one-dimensional ANSYS-AUTODYN. J Energ Mater 29(4):292–325

69. Mair HU (1999) Hydrocodes for structural response to underwater explosions. Shock Vib 6 (2):81–96
70. Teeling-Smith R, Nurick G (1991) The deformation and tearing of thin circular plates subjected to impulsive loads. Int J Impact Eng 11(1):77–91
71. Nurick G, Gelman M, Marshall N (1996) Tearing of blast loaded plates with clamped boundary conditions. Int J Impact Eng 18(7–8):803–827
72. Espinosa HD, Lee S, Moldovan N (2006) A novel fluid structure interaction experiment to investigate deformation of structural elements subjected to impulsive loading. Exp Mech 46 (6):805–824
73. Rajendran R, Paik J, Lee J (2007) Of underwater explosion experiments on plane plates. Exp Tech 31(1):18–24
74. Houlston R, Slater J (1991) Global and local modelling of naval panels subjected to shock loads. Comput Struct 40(2):353–364
75. Houlston R, Slater J (1993) Damage analysis with ADINA of naval panels subjected to a confined air-blast wave. Comput Struct 47(4–5):629–639
76. Jiang J, Olson M (1991) Nonlinear dynamic analysis of blast loaded cylindrical shell structures. Comput Struct 41(1):41–52
77. Kambouchev N, Noels L, Radovitzky R (2006) Nonlinear compressibility effects in fluid-structure interaction and their implications on the air-blast loading of structures. J Appl Phys 100(6):063519
78. Kambouchev N, Noels L, Radovitzky R (2007) Numerical simulation of the fluid–structure interaction between air blast waves and free-standing plates. Comput Struct 85 (11–14):923–931
79. Kambouchev N, Radovitzky R, Noels L (2007) Fluid–structure interaction effects in the dynamic response of free-standing plates to uniform shock loading. J Appl Mech 74 (5):1042–1045
80. Gupta N (2007) Deformation and tearing of circular plates with varying support conditions under uniform impulsive loads. Int J Impact Eng 34(1):42–59
81. Louca L, Pan Y, Harding J (1998) Response of stiffened and unstiffened plates subjected to blast loading. Eng Struct 20(12):1079–1086
82. Ramajeyathilagam K, Vendhan C (2004) Deformation and rupture of thin rectangular plates subjected to underwater shock. Int J Impact Eng 30(6):699–719
83. DeRuntz J (1989) The underwater shock analysis code and its applications, In 60th shock and vibration symposium proceedings
84. Hammond L, Grzebieta R (2000) Structural response of submerged air-backed plates by experimental and numerical analyses. Shock Vib 7(6):333–341
85. Abrate S (1997) Localized impact on sandwich structures with laminated facings. Appl Mech Rev 50(2):69–82
86. Hall D (1989) Examination of the effects of underwater blasts on sandwich composite structures. Compos Struct 11(2):101–120
87. McCoy R, Sun C (1997) Fluid-structure interaction analysis of a thick-section composite cylinder subjected to underwater blast loading. Compos Struct 37(1):45–55
88. Hassan N, Batra R (2008) Modeling damage in polymeric composites. Compos Part B-Eng 39 (1):66–82
89. Batra R, Hassan N (2008) Blast resistance of unidirectional fiber reinforced composites. Compos Part B-Eng 39(3):513–536
90. Batra RC, Hassan NM (2009) Modeling of progressive damage in high strain—rate deformations of fiber-reinforced composites. In: Major accomplishments in composite materials and sandwich structures. Springer, Dordrecht, pp 89–111
91. Batra R, Hassan N (2007) Response of fiber reinforced composites to underwater explosive loads. Compos Part B-Eng 38(4):448–468

92. Nezami M, Jam J, Nia N (2009) Dynamic response of free–free laminated curved panels subjected to explosive blast. Polym Compos 30(9):1199–1203
93. LeBlanc J, Shukla A (2010) Dynamic response and damage evolution in composite materials subjected to underwater explosive loading: an experimental and computational study. Compos Struct 92(10):2421–2430
94. LeBlanc J, Shukla A (2011) Dynamic response of curved composite panels to underwater explosive loading: experimental and computational comparisons. Compos Struct 93 (11):3072–3081
95. Russell DM (1997) Error measures for comparing transient data: Part I, development of a comprehensive error measure. In: Proceedings of the 68th shock and vibration symposium. Shock and Vibration Exchange, Hunt Valley
96. Mäkinen K (1999) The transverse response of sandwich panels to an underwater shock wave. J Fluid Struct 13(5):631–646
97. McMeeking RM, Spuskanyuk A, He M, Deshpande V, Fleck N, Evans A (2008) An analytic model for the response to water blast of unsupported metallic sandwich panels. Int J Solid Struct 45(2):478–496
98. Librescu L, Nosier A (1990) Response of laminated composite flat panels to sonic boom and explosive blast loadings. AIAA J 28(2):345–352
99. Librescu L, Oh SY, Hohe J (2004) Linear and non-linear dynamic response of sandwich panels to blast loading. Compos Part B-Eng 35(6–8):673–683
100. Wei Z, Dharmasena K, Wadley H, Evans A (2007) Analysis and interpretation of a test for characterizing the response of sandwich panels to water blast. Int J Impact Eng 34 (10):1602–1618
101. Wadley H, Dharmasena K, Chen Y, Dudt P, Knight D, Charette R, Kiddy K (2008) Compressive response of multilayered pyramidal lattices during underwater shock loading. Int J Impact Eng 35(9):1102–1114
102. Panahi B, Ghavanloo E, Daneshmand F (2011) Transient response of a submerged cylindrical foam core sandwich panel subjected to shock loading. Mater Des 32(5):2611–2620
103. Gopinath G, Batra RC (2018) A common framework for three micromechanics approaches to analyze elasto-plastic deformations of fiber-reinforced composites. Int J Mech Sc 148 (2018):540–553
104. Batra RC, Gopinath G, Zheng JQ (2012) Damage and failure in low energy impact of Fiber-reinforced polymeric composite laminates. Compos Struct 94:540–547
105. Robertson DD, Mall S (1994) Micromechanical analysis for thermo-viscoplastic behavior of unidirectional fibrous composites. Compos Sci Technol 50:483–496
106. Batra RC et al. (2018) Unpublished results
107. Batra RC, Xiao J (2013) Finite deformations of curved laminated St. Venant-Kirchhoff beam using layer-wise third order shear and Normal deformable beam theory (TSNDT). Compos Struct 97:147–1614
108. Taetragool U, Shah PH, Halls VA, Zheng JQ, Batra RC (2017) Stacking sequence optimization for maximizing the first failure initiation load followed by progressive failure analysis until the ultimate load. Compos Struct 180:1007–1021
109. Qin Z, Batra RC (2009) Local slamming impact of sandwich composite hulls. Int J Solid Struct 46(10):2011–2035
110. Das K, Batra RC (2011) Local water slamming impact on sandwich composite hulls. J Fluid Struct 27(4):523–551
111. Xiao J, Batra RC (2014) Delamination in sandwich panels due to local water slamming loads. J Fluid Struct 48:122–155
112. Qu Y, Batra RC (2017) Constrained moving least-squares immersed boundary method for fluid-structure interaction analysis. Int J Numer Methods Fluids 85(12):675–692

113. Monasse L, Daru V, Mariotti C, Piperno S, Tenaud C (2012) A conservative coupling algorithm between a compressible flow and a rigid body using an embedded boundary method. J Comput Phys 231:2977–2994
114. Pasquariello V, Hammerl G, Örley F et al (2016) A cut-cell finite volume–finite element coupling approach for fluid–structure interaction in compressible flow. J Comput Phys 307:670–695
115. Qu Y, Shi R, Batra RC (2018) An immersed boundary formulation for simulating high-speed compressible viscous flows with moving solids. J Comput Phys 354:672–691